

Seylamouni Lecomte-Saur

Measurement and analysis of a membrane energy exchanger for energy efficient ventilation

Master's thesis in Sustainable Energy Use in Buildings

Supervisor: Hans Martin Mathisen, Liu Peng

July 2020

Seylamouni Lecomte-Saur

Measurement and analysis of a membrane energy exchanger for energy efficient ventilation

Master's thesis in Sustainable Energy Use in Buildings
Supervisor: Hans Martin Mathisen, Liu Peng
July 2020

Norwegian University of Science and Technology
Faculty of Engineering
Department of Energy and Process Engineering



Preface

The Master thesis was conducted at the Department of Energy and Process Engineering at the Norwegian University of Science and Technology, Trondheim. The thesis represents 30 ECTS for the spring semester and is the continuation of the semester project work conducted during the fall. Some of the previous work will be used in this thesis. This work is carried out as part of the research project Defreeze MEE Now. Defreeze MEE Now is an industry-owned project with NTNU and SINTEF as the research partners.

The master thesis agreement mostly featured experimental work and also comprised a simulation part. However, the experimental work had to be interrupted due the Coronavirus. On the 12th of March, the university was closed for several weeks and all lab access was forbidden. Consequently, the thesis plan was modified in cooperation with my supervisors to be able to complete the thesis. The work is therefore centered on simulation, using the results I had time to produce in the lab.

I would like to thank my supervisor Prof. Hans Martin Mathisen and my co-supervisor Liu Peng, PhD, for their regular guidance which helped me understand the subject and overcome challenges. I am especially grateful for their support in difficult situations, when I changed my choice of project late in the fall semester, and when the lockdown due to the Coronavirus kept me from continuing my experiments.

My gratitude goes also to Inge Håvard Rekstad and Lars Konrad Sørensen for helping me fix the experimental rig and teaching me how to use it.

Finally, I would like to thank my friend Susan Lyimo for her help and her constant support and friendship.

Seylamouni Lecomte-Saur, Msc. student.
Department of Energy and Process Engineering,
Norwegian University of Science and Technology, Trondheim, June 2020.

Project description

Master thesis

for

Student Seylamouni Lecomte-Saur

Spring 2020

Measurement and analysis of a membrane energy exchanger for energy efficient ventilation

In order to save energy, buildings are requested to have larger air-tightness. In order to provide sufficient indoor air quality, mechanical ventilation remains as the only solution. However, ventilation systems require large amounts of energy mostly related to the heating of the supply air. As a solution to that, heat recovery is a common practice, though this does not use all the potential energy related to latent energy. Besides, in recuperative heat exchangers there is a big risk for frost, due to condensation of the moisture in exhaust air on the exchanger's surface. Therefore, the goal of this thesis is to analyse membrane energy exchangers that enable latent and sensible energy recovery. Experimental work that has been conducted will be used to establish correlations for use in a model to determine effectiveness and pressure drop. The model can be extended to calculate yearly energy savings in a virtual house for different locations. A parametric analysis can be conducted to analyse the influence of different factors.

The master thesis plan was modified because access to the lab was forbidden during the semester due the Coronavirus lockdown. Above is the plan that was decided on to adapt to the situation. It is more focused on simulation than the previous one, which was focused on experiments.

Abstract

Energy recovery is an essential energy-saving measure for buildings with mechanical ventilation. In cold climate, a common issue with the widely used flat-plate heat exchanger is the condensation of moisture in exhaust air and formation of frost in the exchanger. The need for defrosting consumes energy and may intermittently reduce indoor air quality. A solution to reduce or eliminate frost formation is to use membrane energy exchangers (MEE), which can transfer water vapor as well as sensible heat between the exhaust and supply air streams.

The use of membranes instead of impermeable plates creates a need for spacers in between the membranes, to support the thin membranes and avoid deformation of the air channels, which can undermine performances. The spacers influence the performances of the MEE: they can enhance heat and moisture transfer, resulting in higher effectiveness, but they also increase pressure drop, resulting in more energy consumed by the fans. Although many studies have been conducted to measure and predict the performances of MEEs in hot and humid climate, fewer have been conducted in cold climate, and very few have investigated the influence of different types of spacers.

In this thesis, a literature study is presented on the latest developments of membrane energy exchanger technology. Experimental work has been conducted to measure the performances of a MEE with one type of spacer under different conditions of temperature, relative humidity and air flow rate. Then, a ϵ -NTU model was created using MATLAB, validated against the experimental data, and used to predict the performances of the MEE with different spacers, different geometries, and calculate the potential energy savings in different Norwegian cities: Trondheim, Bergen and Oslo.

It was found that for the three cities the choice of spacer and geometry is of significant importance to maximise energy savings. Although there is a trade-off, as denser spacers both enhance heat and moisture transfer and increase pressure drop, it seems that pressure drop is predominant in limiting energy savings, especially when fan efficiencies are low. The orientation, corrugation size and corrugation shape of the spacers are factors that may contribute significantly to reducing or increasing the pressure drop, as well as the length and width of the exchanger. These factors will have to be investigated experimentally to confirm the results of this thesis.

Contents

Preface	i
Project description	iii
Abstract	v
List of Tables	xi
List of Figures	xiv
Nomenclature	xiv
1 Introduction	1
1.1 Context	1
1.2 Heat recovery and the quasi-counter flow membrane enthalpy exchanger	2
1.2.1 Indoor air quality and heat recovery	2
1.2.2 The membrane energy exchanger	4
1.3 Objectives and scope	5
1.3.1 Objectives	5
1.3.2 Scope	6
2 Literature review	7
2.1 Recent developments	7
2.1.1 Frosting	7
2.1.2 Performance analysis	8
2.1.3 Performances of different types of membranes	10
2.2 Studies used in this project	11
3 Theory	13
3.1 The ϵ -NTU method to predict effectiveness	13
3.2 Sensible heat transfer coefficient U_s	14
3.2.1 Convective heat transfer coefficient h	15

3.3	Moisture transfer coefficient U_l	15
3.3.1	Convective moisture transfer coefficient k for an empty channel	16
3.3.2	Moisture diffusion resistance of the membrane r_{mm}	17
3.4	Pressure drop	18
3.4.1	Core pressure drop for the fully developed flow in the cross- and counter-parts	19
3.4.2	Entrance and exit pressure drop	20
3.4.3	Pressure drop due to bends	21
3.4.4	Total pressure drop	21
3.5	Channel with spacer	22
3.5.1	Heat and mass transfer	22
3.5.2	Pressure drop	23
4	Measurements	25
4.1	Test rig	25
4.2	Measurements devices	26
4.2.1	Thermocouples and relative humidity sensors	26
4.2.2	Manometers	26
4.3	Measurement of flow with orifice plates	28
4.4	Data acquisition and treatment	29
4.4.1	Effectiveness and Colburn factor	29
4.4.2	Pressure drop and friction factor	31
4.5	Uncertainty analysis	32
4.5.1	Temperature and moisture content	33
4.5.2	Sensible and latent effectiveness	34
4.5.3	Resulting uncertainties	34
4.6	Propositions for new spacers	35
5	Model	37
5.1	Description of the modelled installation	37
5.2	Correlations for Colburn j factor and friction factor f	39
5.2.1	Influence of spacer angle	39
5.2.2	Influence of corrugation pitch	41
5.3	Verification of model against experimental data	42
5.4	Energy savings calculations	42
6	Results and discussion	45
6.1	Experiments results	45
6.2	Model results	46
6.2.1	Parametric analysis	47
6.3	Advantages and limitations of the model	52
7	Conclusions and further work	55
	Bibliography	57

Appendix A: Risk assessment	60
Appendix B: Calculation of membrane diffusivity	64
Appendix C: KaysEff function	65
Appendix D: E2NTU function	66
Appendix E: f and j correlations for angled spacer	67
Appendix F: MEE with “Lab” spacer	69
Appendix G: Yearly savings calculation	71
Appendix H: Parameters used in the model	73
Appendix I: Measurement data, Case 025	74
Appendix J: Measurement data, Case 030	75
Appendix K: Measurement data, Case 040	76
Appendix L: Measurement data, Case 530	77
Appendix M: Effectiveness-RHei regression	78

List of Tables

1.1	Comparison of different exchangers [18, 19, 31].	4
3.1	Effectiveness of the quasi-counterflow exchanger as function of the NTU in the counter- and cross- parts [13].	14
4.1	Measurement devices.	27
4.2	Parameters used in orifice plate air flow rate calculation.	28
4.3	Pressure drop measurement across orifice plate and calculated air flow rate.	28
4.4	Uncertainties for Case 030 at 3.4 L/s.	34
5.1	Characteristics of the model	38
5.2	Properties of the spacers	39
5.3	Energy calculations for all the possible outdoor conditions	43
7.1	Values given by the manufacturer	64

List of Figures

1.1	A schematic of ventilation and heat recovery in a house.	3
1.2	A heat wheel (a) and a flat-plate heat exchanger (b).	3
1.3	Shape of counter- cross- and quasi-counterflow exchangers	5
3.1	Simplification of the flow pattern	19
3.2	Pressure profile for an air stream entering and exiting a channel.	20
3.3	Correlation between $K_{L,bend}$ and aspect ratio α for a 45°bend	21
3.4	Pressure drop numbers used in the calculations for $\sigma = 0.5$ [29, 1].	21
3.5	Temperature boundary layer build-up in laminar flow.	22
3.6	Boundary layer with and without spacer.	23
3.7	Flow direction through the spacer.	23
4.1	Schematic of the test rig.	25
4.2	Split view of the exchanger core.	26
4.3	Dimensions of the exchanger core.	26
4.4	Manometer correlations	27
4.5	Measured effectiveness for Case 025 and Case 040.	30
4.6	Measured effectiveness for Case 030 and Case 530.	30
4.7	Effectiveness for the total NTU, with $NTU_x/NTU_c = 0.3125$	31
4.8	Experimental Colburn factor	31
4.9	Experimental Darcy friction factor	32
4.10	Fabrication steps	35
5.1	Schematic of the installation	37
5.2	Spacers used in the model	39
5.3	Dimensions for hydraulic diameter calculation.	39
5.4	Correlations from Woods	40
5.5	Friction factor correlations from Retterstøl [28]. d =corrugation pitch p	41
5.6	Comparison of model results and experimental results	42
5.7	Temperature and moisture content labels.	43

6.1	Experimental effectiveness results against indoor relative humidity and supply inlet temperature conditions.	46
6.2	Energy savings and energy consumption results from the model.	46
6.3	Shape of the MEE with different a/L ratios.	48
6.4	Effectiveness with increasing share of NTU in the counter-part. From Kays et al. [13].	48
6.5	Performances of the MEE with varying a/L ratio and constant transfer area.	49
6.6	Performances of the MEE with varying channel spacing b and constant flow rate.	50
6.7	Performances of the MEE with varying hydraulic diameter.	51
6.8	Hydraulic diameter of trapezoidal channel with varying beta angle, constant height=2mm and constant width=20mm (long side).	52
6.9	Effectiveness from the KaysEff function (Appendix C).	52
7.1	Linear regression for effectiveness versus RH_{ei}	78

Nomenclature

Parameters

\dot{m}	Mass flow rate [kg/s]
A	Area of the surface of exchange in the heat exchanger [m^2]
a	Width of the counter part [m]
b	Channel spacing [m]
C	Heat capacity [J/K]
c_p	Specific heat capacity of air at constant pressure [$J/(kg.K)$]
D_v	Diffusivity of water vapor in air [m^2/s]
D_h	Hydrodynamic diameter of an air channel [m]
D_p	Diffusivity of porous membrane [m^2/s]
f	Fanning friction factor
G	Specific mass flow rate [$kg/m^2.s$]
g_c	Proportionality constant in Newton's second law of motion [$g_c = 1$ in <i>SI units</i>]
H	Enthalpy [J]
h	Convective heat transfer coefficient [W/m^2K]
J	Volume flux of water vapor [$m^3/(m^2.s)$]
j	Colburn factor
k	Convective moisture transfer coefficient [m/s]
L	Length of the counterflow part [m]

P	Pressure [Pa]
P_v	Water vapor partial pressure [Pa]
P_{sat}	Saturation pressure of water vapor in air [Pa]
Q	Energy consumed or saved [J]
q	Heat transfer rate [W]
r_{mm}	Membrane moisture diffusion resistance [s/m]
T	Temperature [$^{\circ}C$]
t	Time [s]
U	Overall heat/mass transfer coefficient [$W/(m^2K)$]
w	Humidity ratio [kg/kg]

Acronyms

MEE	Membrane energy/enthalpy exchanger
NTU	Number of Transfer Units
RH	Relative humidity

Greek letters

α	Aspect ratio
Δh_{lv}	Specific vaporization enthalpy of water [J/kg]
Δp	Pressure drop [Pa]
ΔT	Temperature difference [K]
δ	Membrane thickness [m]
ϵ	Effectiveness
λ	Thermal conductivity [$W/(m.K)$]
μ	Dynamic viscosity [$kg/(m.s)$ or $Pa.s$]
ν	Kinematic viscosity [m^2/s]
ρ	Density of air [kg/m^3]

Non-dimensional numbers

Le	Lewis number
Nu	Nusselt number

<i>Pr</i>	Prandtl number
<i>Re</i>	Reynolds number
<i>Sc</i>	Schmidt number
<i>Sh</i>	Sherwood number
<i>St</i>	Stanton number
<i>St_m</i>	Mass Stanton number

Subscripts

<i>a</i>	Air
<i>c</i>	Counter-like part
<i>ei</i>	Exhaust inlet
<i>eo</i>	Exhaust outlet
<i>h</i>	Hydraulic (hydraulic diameter)
<i>l</i>	Latent
<i>m</i>	Membrane, moisture, mean, mass
<i>max</i>	Maximum
<i>min</i>	Minimum
<i>s</i>	Sensible
<i>si</i>	Supply inlet
<i>so</i>	Supply outlet
<i>v</i>	Water vapor
<i>wv</i>	Water vapor
<i>x</i>	Cross-like part

Introduction

1.1 Context

The latest IPCC reports estimated that to keep global warming below 1,5°C above pre-industrial levels, anthropogenic CO₂ emissions have to be net zero by 2050 and be well reduced by 2030 [33]. Every additional fraction of degree of warming is decisive in determining the lives of people across the world. Thus, it is vital to halt climate change. As greenhouse gas emissions are mostly driven by fossil energy consumption, reducing the global energy consumption is an important feature of climate mitigation plans. In 2018, the buildings and construction sector accounted for 36% of final energy use and 39% of emissions related to energy and processes [34] with 50% or more energy savings potential globally. There is therefore great energy saving potentials in buildings, and particularly in the conditioning of ventilation air, once the building envelope is improved. Indeed, in cold climate, energy consumption for heating of the ventilation air can be as high as 60% of the annual total energy consumption [12].

To avoid heat losses through infiltration of outdoor air, buildings are becoming more airtight, and thus require mechanical ventilation systems to achieve satisfactory indoor air quality. Mechanical ventilation is also an opportunity for heat recovery, which has the potential to achieve substantial energy savings, up to 20% of primary energy use [12]. Heat recovery is achieved by using components that are called heat or energy exchangers, which are used in ventilation systems to transfer heat from one air stream to the other. some of the most widely used heat recovery exchangers are the flat-plate heat exchanger and the rotary wheel energy exchanger.

One of the main limitations to the performance of heat exchangers in cold climate is the formation of frost due to condensation and freezing of the moisture contained in the warm and humid indoor air. The formation of frost decreases the air flow in the exchanger and the heat transfer, which reduces performances. The exchanger can also be damaged if there is too much frost formation. Hence there is a requirement for a defrosting system, which consumes energy, increases investment cost and can reduce indoor air quality [8]. To reduce the need for defrosting, in the recent years flat-plate energy exchangers with

membranes instead of metal or plastic plates have been studied for application in cold climate [18, 8]. The membranes selectively let water vapor through and block pollutants. As a result, the membrane transfers both sensible heat and latent heat (water vapor). Such exchangers can be called membrane energy/enthalpy exchangers (MEE) or membrane energy recovery ventilators (MERV) when the fans are included. Initially, membranes were introduced for energy recovery applications in hot and humid climate, where the conditioning of supply air is also very energy intensive, due to the need for cooling and dehumidification [37]. In cold climate, symmetrically, the desire is to transfer heat and humidity from the warm and humid exhaust air to the cold and dry supply air, to reduce heating demand and prevent condensation and frosting on the supply side. Another advantage is that it reduces the discomfort often caused by supply air dryness [18].

1.2 Heat recovery and the quasi-counter flow membrane enthalpy exchanger

1.2.1 Indoor air quality and heat recovery

The ASHRAE defines acceptable indoor air quality (IAQ) as [6]:

Acceptable indoor air quality: air in which there are no known contaminants at harmful concentrations as determined by cognizant authorities and with which a substantial majority (80 % or more) of the people exposed do not express dissatisfaction.

Different sources emit pollutants to the air in a building : building materials, people and activities. It is therefore essential to have the indoor air renewed regularly to keep sufficient indoor air quality. This was historically done by infiltration and natural ventilation (eg. opening of windows). However infiltration of outdoor air through the building envelope causes substantial heat losses, and the current building regulations require building envelopes to be airtight. The Norwegian building code TEK17 requires residential buildings to have an infiltration number under 1.5 air changes per hour for 50 Pa pressure difference [32]. Therefore mechanical ventilation, which uses fans and ducts to provide fresh air to different parts of the building, is required to maintain satisfactory IAQ.

The incoming fresh air needs to be conditioned to be supplied with comfortable levels of temperature and humidity. This can be very energy intensive, especially in hot climate and cold climate. Thus, energy recovery technologies are also required by the building code to have an efficiency over 80% [32]. These heat/energy exchangers can transfer heat from one air stream to the other, while limiting the transfer of pollutants (fig. 1.1). Exchangers may be referred to as heat or energy exchangers. The designation differs according to the type of energy that is recovered. Heat exchangers only recover sensible heat, while energy exchangers have the possibility to recover both sensible heat and latent heat, that is water vapor.

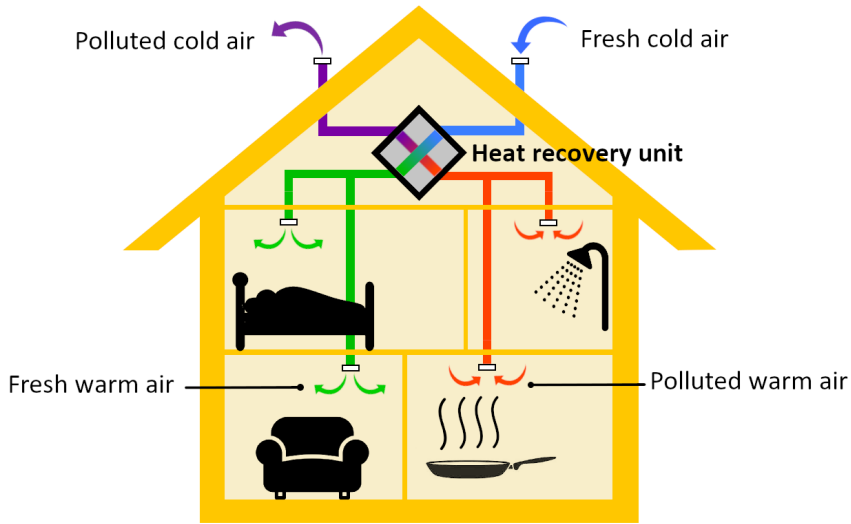


Figure 1.1: A schematic of ventilation and heat recovery in a house.

Two of the most widely used exchangers are the energy wheel, which is an energy exchanger and the cross-flow flat-plate heat exchanger. Advantages of the energy wheel are a high effectiveness, and the possibility to recover moisture, which ensures a lower frosting limit. However, it requires energy and a more complex installation to have a rotating wheel, and there is a possibility of cross-contamination, as the supply and exhaust air go through the same channels in the wheel (fig. 1.2). On the other hand, advantages of the cross-flow flat-plate heat exchanger are a simple installation with no moving parts and no cross-contamination as the channels are physically separated. The drawbacks are no moisture transfer, and so higher risk of frost formation, which hinders the performances in cold climate [31].

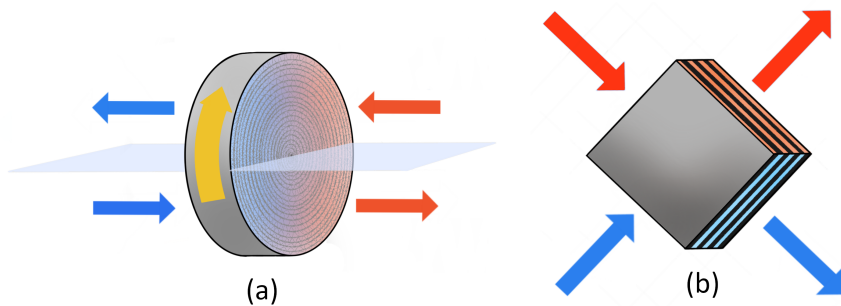


Figure 1.2: A heat wheel (a) and a flat-plate heat exchanger (b).

1.2.2 The membrane energy exchanger

The membrane energy exchanger is similar to a flat-plate heat exchanger with membranes instead of the metal or plastic plates. The membranes are selectively permeable to water vapor and block other pollutants. Therefore, MEEs combine the simplicity of flat-plate heat exchangers with the possibility of moisture transfer. Table 1.1 shows a comparative summary of the properties of the energy wheel, the flat-plate cross-flow and the membrane quasi-counterflow exchanger.

The table shows that, additionally to combining sensible and latent heat transfer with the simple flat-plate structure, membrane quasi-counterflow exchanger has the potential to have higher effectiveness than that of an energy wheel. However, although theoretically the membranes should prevent cross-contamination, the selectivity (i.e. the pollutant-blocking qualities of the membranes) still needs to be further investigated [11]. The frosting limit, which is of importance for design in cold climate, is also mentioned in the table. The frosting limit is defined as the combination of indoor and outdoor conditions at which frost starts to form in the exchanger [19]. Indoor relative humidity and outdoor temperature are identified as the main variables defining the frosting limit. In the table, frosting limits outdoor temperatures are given for a fixed value of relative humidity. For membrane energy exchanger, the frosting limit temperature is very dependent on the exhaust relative humidity, so the temperature given in the table may not be representative of the whole range but is given as an example.

Table 1.1: Comparison of different exchangers [18, 19, 31].

	Energy wheel	Flat-plate Cross-flow	Membrane Quasi-counterflow
Energy recovered	Heat and moisture	Sensible heat	Heat and moisture
Structure	Rotating wheel requires a motor	No moving parts	No moving parts
Cross-contamination	Possible	No	No
Sensible effectiveness	50-85%	60-80%	80->90% [22, 18]
Latent effectiveness	50-85%	No	46-82% [22, 18]
Frosting limit at 30% RH	-29°C	<-5°C	-8°C*

*The frosting limit temperature is heavily dependent on RH for membrane energy exchangers.

A quasi-counterflow shape for higher effectiveness

The three basic flow configurations for heat/energy exchangers are: parallel flow, crossflow and counterflow. Parallel flow is never used in practice as it gives a lower effectiveness. Crossflow is very common, although theoretically the counterflow configuration gives the highest effectiveness. That is because in practice it is difficult to install the ducting on a pure counterflow exchanger as the supply and exhaust channels are on the same face (see fig. 1.3). A good compromise is the quasi-counterflow shape, which combines a counterflow body with crossflow headers for connections to the ducting. This configuration can increase the effectiveness: crossflow shapes typically have an effectiveness between 60%

and 80% and it was found that prototypes of quasi-counterflow MEEs can exceed 90% for sensible effectiveness [20, 22].

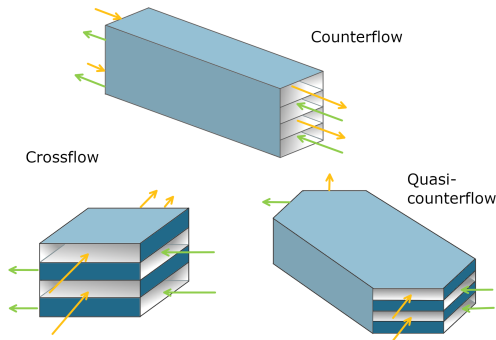


Figure 1.3: Shape of counter- cross- and quasi-counterflow exchangers

Spacers to avoid deflection and enhance heat and moisture transfer

Unlike metal plates, membranes are very thin and flexible. Pressure differences on each side of the membrane can easily deflect it, causing a channel to be either enlarged or obstructed, which is detrimental to the performances of the MEE. Thus, spacers are required between the membranes to maintain the shape of the channels. They are often made of corrugated wire mesh, and research is being conducted on the use of other types of materials [25]. The presence of a spacer usually improves heat and mass transfer, but it also increases pressure drop, which in turn increases the energy consumed by fans. Therefore, it is important to design spacers with low pressure drop to maximize energy savings.

1.3 Objectives and scope

1.3.1 Objectives

The objectives of this thesis are to:

1. Conduct a literature study centered on the performances of MEEs, particularly in cold climate.
2. Experimentally measure the effectiveness and pressure drop of a MEE prototype.
3. Use the measurements to establish correlations for use in an effectiveness and pressure drop model of the MEE, validate the model against experiments.
4. Use previous studies to make an informed guess on the performances of the MEE with different spacers.
5. Extend the model to calculate annual energy savings for a house in different cities.

6. Perform a parametric analysis to find how the geometrical configuration of the MEE can be optimized.

1.3.2 Scope

The goal of this thesis is to cover the performances of membrane energy exchangers, in terms of energy savings, under different conditions, and to find how the configuration can be optimized. Other types of exchangers can be mentioned but will not be modelled, as the objective is to compare different configurations of the same MEE. The performances regarding indoor environment quality are also outside the scope of this thesis, as is the time-response of the MEE. Consequently, all the models are static and heat and mass transfer are explained assuming steady-state. Conjugate effects of heat and mass transfer are acknowledged but not included in the model.

Literature review

This chapter presents an overview of recent research that has been conducted on MEEs. Scientific articles have been included if the publication year was after 2010 and based on the author's appreciation of their relevance to the subject. The chapter is divided into two sections: the first one presents recent developments in the field of MEEs, the second one presents the articles that have been actively used in this thesis. Most of the articles that have been chosen are experimental and/or CFD studies of the performances of MEEs in different conditions, or development/assessment of performance prediction methods. Separate sections have been created for the investigation of frosting in MEEs and for the testing of different types of membranes.

The results from these studies mostly agree with each other. The studies that compared energy savings with MEEs and with heat exchangers all found that the savings were higher with MEEs [8, 24, 21, 30]. It also seems that the flow configurations giving the best performances are Z-shape and quasi-counterflow shape [3, 4]. When studying the influence of outdoor condition however, some discrepancies can be found between the findings. Kho et al., Beattie et al., Liu et al. and Albdoor et al. found little to no influence of outdoor temperature on effectiveness; Albdoor et al. and Al-Waked et al. found that the latent effectiveness was dependent on outdoor humidity; but Choi et al. found sensible and latent effectiveness to be very variable depending on outdoor conditions [15, 8, 22, 5, 2, 10]. Finally, all the studies that featured spacers observed that spacers enhance heat and mass transfer, but that they also increase pressure drop. However, whether the trade-off is in favor of spacers or not is not unanimous [15, 3, 16].

2.1 Recent developments

2.1.1 Frosting

While in warm climate the main advantage of moisture transfer is to save energy on the dehumidification of the air, in cold climate the main advantage of the moisture transfer through the membrane is to reduce/avoid frost formation in the exchanger. The interest

for MEEs in cold climate is developing, and more publications can be found from the last decade than from the previous one. However, on specific aspects of MEEs like frost formation, the research can be sparse. Rafati Nasr et al. (2014), in their review on frosting in air-to-air energy exchanger [27], reported no work on frosting in membrane energy exchangers.

Since then, Liu et al. (2017) investigated frosting limits for a cross-flow membrane energy exchanger arrangement [20] and for a quasi-counter flow arrangement [19]. They found that their model was consistent with experimental results, and in both cases that the moisture transfer was determinant to the limit of the frosting conditions. In the case of the quasi-counter flow arrangement, they have shown that the diffusive moisture transfer resistance of the membrane had much more influence on the frosting limits than airflow rates, exhaust air temperatures and channel spacing. Therefore they recommend the use of membranes with high moisture transfer rates, to have the maximal range of frost-free operating conditions.

More recently Beattie et al. (2018) conducted a study of frost formation on different types of exchanger cores and proposed a system with parallel exchangers [8]. They found that the MEEs froze at much lower temperature than the heat exchanger with impermeable plates. They also found differences among the membrane cores. The polymerized paper membrane core showed the best performances, with considerably less airflow reduction due to frost than the cores with membrane substrate and vapor-permeable coating. For example, at -25°C and after two hours of continuous operation, the polymerized paper core experienced a reduction of airflow rate of 4.4%, while the two cores with substrate and coating had 21.7%, and 23.5%, and the sensible-only core had 29.9%. Beattie et al. developed a commissioning method to replace the operation model from the manufacturer with one that is more adapted to the specific conditions of the installation. Correlations from frost tests were used to make the new model for defrosting schedule. With the scheduled operation, all cores had the same sensible effectiveness, at all the temperatures tested (-5°C to -35°C), but during defrosting periods there is no air supply. The proposed solution is to switch between two cores in parallel for operation/defrosting, so that the indoor air quality stays constant.

2.1.2 Performance analysis

Kho et al. (2017) created a CFD model of a quasi-counter flow MEE [15]. They tested the influence of having ribs in the flow channel versus having an empty channel. They found that the ribs helped heat and moisture transfer as the velocity increases, but also that it makes the increase in pressure drop with velocity much steeper than with the empty channel. They tested the effect of outdoor air temperature and humidity on sensible and latent effectiveness, and did not find significant effect. They also investigated the effect of channel height on sensible and latent effectiveness and pressure drop. they found that there could be a trade-off, as a thinner channel improves effectiveness but also increases pressure drop.

Al-Waked et al. (2015) conducted a CFD study of MEEs with variable membrane moisture resistance using FLUENT. They implemented a user define function (UDF) in the model to simulate the variation of membrane moisture resistance with variations in humidity, based on equations from literature. They tested the function with a cross-flow ex-

changer simulation and found that the membrane moisture resistance could vary between 14 and 25 s/m and that the variations were smaller at higher flow rates, due to shorter residence time and thus mass fraction difference remaining high across the membrane. They validated their model against previous studies and simulated exchangers with the three basic flow configurations (parallel-, cross- and counter-flow) and two different membranes. They found that the type of membrane had little influence on the performances compared to the flow configuration. They also found that the total hydraulic diameter (the sum of hydraulic diameters on both sides of the membrane) was of significant importance to the conjugate heat and mass transfer.

Al-Waked et al. conducted another CFD study in 2018 of the thermal performance of a membrane based ERV under turbulent flow conditions [3]. They investigated different conditions and configurations, and found that the highest performing configuration was straight shape for cold air and Z-shape for warm air, but the quasi-counter flow layout had also shown high performance and may be preferable depending on the configuration of the whole system. They found that face velocity is almost 5 times more important than flow separators with regards to affecting the thermal performance. However channel separators are still an important element as they can improve thermal performance by up to 8.7%, and provide support and stability. As Kho et al., they confirmed that more channel separators induce higher thermal performance, but also increase pressure drop.

Albdoor et al. (2020) measured the properties of different membranes, then used the highest-performing membrane to construct an exchanger [4]. Different flow configuration were tested and they found the configuration that gave the highest performances. They conducted an experimental performance comparison between six different hybrid configurations. By partially obstructing the entrance of the cross-flow channels, they could obtain “mixed” flow configurations: cross-flow configuration (entrance ratio = 1), and Z-shapes (entrance ratio 0.75, 0.50, and 0.25). Their results showed that lower entrance ratio gave higher effectiveness but also higher pressure drop. However as fan energy consumption is much lower than the energy transferred, the highest capacity for energy recovery was with Z-shape supply and exhaust, with entrance ratio 0.25, which gave a 14.6% increase in total effectiveness compared to pure crossflow.

Choi et al. (2018) studied the influence of having a constant efficiency for an ERV in building energy simulations. They performed field measurements over 20 days in a house in winter conditions in Korea. The studied area had one cross-flow membrane energy exchanger located in the window frame, for which they measured the sensible, latent and total effectiveness. They found that the sensible effectiveness varied between 30% and 65% depending on outdoor conditions, the latent effectiveness varied between 25% and 70%, and both were lower than the prescriptive value from the manufacturer. Thus the total efficiency was not constant as prescribed and was observed to be mostly influenced by changes in the outdoor air temperature rather than outdoor humidity. They made a simulation in TRNSYS and compared two cases: one using constant effectiveness and the other using a variable effectiveness based on the correlations found in the field measurements. They found that the heating demand was 69% higher with the variable effectiveness, showing that using a constant effectiveness for building energy simulations may lead to an underestimation of the heating demand.

Zhong et al. (2015) constructed an optimized plate-fin total exchanger (PFTHE) and

measured its sensible and latent effectiveness. The exchanger was optimized with an air deflector and air spreader plate. The latent and sensible effectiveness were measured for constant outdoor and indoor temperatures and moisture contents and were found to be improved by the the air spreader plate, though it is not clear what was the measure of optimisation meant.

Nasif et al. (2014) calculated energy and CO₂ emissions savings using a modified HPRate code based on effectiveness and pressure drop measured on a lab exchanger with kraft paper membrane. They calculated energy savings for London, Miami and Tokyo for four seasons separately, and possible yearly CO₂ savings, compared to a conventional system with mixing of fresh and exhaust air. In all cases the energy consumption was lower for the system with MEE. The largest savings were found for Miami in summer, as the exchanger acts both as sensible heat recovery and dehumidifier in humid climate with high latent load. The smallest savings were found for London and Tokyo in winter, as the sensible load is very high. Annually, they found the possible CO₂ savings to be up to 900 kgCO₂, highest for Miami, in mild and humid climate.

Finally, Qiu et al. (2019) developed an energy exchange efficiency prediction approach for membrane cross-flow heat exchangers based on a multivariate polynomial model [26]. The prediction method requires less experimental data and is faster to execute than a detailed numerical calculation method, and presented acceptable deviation from experimental verification (deviation limits within +- 8.0%). Therefore it could be interesting for engineering applications, to predict performances in conditions for which the experimental data are not available.

2.1.3 Performances of different types of membranes

Albdoor et al. (2019) measured the influence of the membrane pore size on the moisture diffusion resistances of different porous membrane [5]. PVDF (Polyvinylidene difluoride), Nylon and PES (Polyethersulfone) membranes, with pore sizes 0.45, 0.22, 0.10 μm were tested at relatively high temperatures (27.5 to 32.5 °C) and 30, 50 and 80% RH, which corresponds to warm and humid climate conditions, using the wet cup method from standard ASTM E96. Then, the effectiveness of a crossflow MEE using these membranes was calculated using a theoretical model to calculate the latent effectiveness. The results showed that the test conditions and the pore size slightly affected the moisture diffusion resistance. There is an increase of the moisture diffusion resistance with the decrease of pore size. The PVDF45 membrane offered the lowest diffusive resistance, while the Nylon10 showed the highest diffusive resistance. They found that the latent effectiveness was not affected much by outdoor temperature but slightly by outdoor humidity.

Paul et al. (2019) tested a manufacturing process to create ribs between the membranes using an adhesive sealant [25]. Instead of using spacers to avoid deflection of the channels, they propose to create a rib pattern by depositing a bead of adhesive sealant on the membrane. A second membrane is then placed on top of the beads, to create the channel, and the two membranes are pulled apart, so that the beads are stretched into thin ribs. Finally, the structure is cured with hot gas. A cost analysis of each step was performed. They found that the manufacturing process was acceptable even though the chosen adhesive was not, as it was wicking compounds into the membrane, which would affect performance.

Baldinelli et al. (2019) investigated the performances of a novel type of organic membrane, SPEEK, compared to a commercial one, Nafion [7]. The membranes are based on crosslinked sulfonated poly(etheretherketone) (XL SPEEK) in acid form. The performances were comparable although those of SPEEK membrane were lower. However, Baldinelli et al. argued that the expected low cost of production could make it competitive.

Xu et al. (2018) investigated the production and performance of sodium alginate membranes [36]. Commonly membranes are made of a hydrophobic substrate with a hydrophilic coating. Sodium alginate as a hydrophilic coating is inexpensive and easy to find, and it has proved to be able to absorb 200-300 times its own weight in water. It has to be cross-linked to reduce water solubility. They made and tested a sodium alginate membrane non-woven fabric. They tested water vapor permeance, water solubility, scanning electron microscope, FT-IR (Fourier Transform Infrared) analysis and simultaneous thermal analysis. The vapor permeance found was up to $29,8 \times 10^{-8} \text{ kg}/(\text{m}^2 \cdot \text{s} \cdot \text{Pa})$, and efficiencies up to 80-87%.

2.2 Studies used in this project

Liu et al. (2016) conducted an experimental study of the performances of a quasi-counterflow MEE [22]. They first predicted the sensible and latent effectiveness by using the ϵ -NTU method, then experimentally measured the sensible and latent effectiveness as well as the pressure drop, and drew correlations for the relation between the friction factor/colburn factor and the Reynolds number. The measurements were done for supply air temperatures between -8°C and 12°C , RH between 20% and 80% and air flow rates of 4,2 l/s, 5,9 l/s and 6,9 l/s. They found that when there is no frost formation, the sensible and latent effectiveness were relatively high and not sensitive to outdoor air temperature, and that the developed model for moisture transfer could give precise estimates. They also found that the optimal channel height for that particular rig was 2mm.

Siegele et al. (2019) studied the performances of a flat plate heat exchanger and a membrane energy exchanger of the same volume. They created both a numerical model on MATLAB and a NTU model with NTU correlations to obtain the effectiveness. They conducted measurements to test the validity of the models. The performances were measured for three different flowrates: $80 \text{ m}^3/\text{h}$, $110 \text{ m}^3/\text{h}$ and $150 \text{ m}^3/\text{h}$. They found that even though the transfer area was larger for the heat exchanger, the heat exchanger and the energy exchanger have comparable enthalpy transfer for both winter and summer conditions. They also found that the NTU method gives good results as long as there is no condensation. In that case, the numerical model should be used.

The ϵ -NTU calculations of this project have been inspired and checked against these studies. The MEE studied in this project has the same overall characteristics as the one used by Liu et al. (2016), with a channel height of 2 mm. Few literature has been found on different kinds of spacers and their influence on the performances, for application in air-to-air exchangers. Woods et al. (2013) conducted a study of the pressure drop and heat transfer enhancement of different kinds of spacers. They measured the pressure drop and heat transfer in a channel with three different spacers at different angles and with different flow rates. They established correlations for the friction factor and the Colburn j factor for each spacer and orientation angle. They also investigated the trade-off between

heat transfer enhancement and pressure drop, and the hypothetical cost savings for an ERV using the same spacers. They found that the triangular plain-fin spacers reduce heat transfer compared to an open channel while the other spacers increase heat and mass transfer. All spacers increase pressure drop. They also observed a transition between steady and unsteady flow for Re between 325 and 550.

Koester et al. (2016) tested four different exchanger cores with the same structure. With two different membranes and one spacer, they tested the module for each membrane with and without spacer. They experimentally measured the effectiveness and pressure drop for each core at different volume flows. Then they performed two different case studies to estimate the energy savings price. They found that while mass transfer was enhanced by the spacer for both of the membranes, heat transfer enhancement varied depending on membrane type and flow rate. Due to increased pressure drop, the cost benefits of having a spacer were found to be little, but potentially of more importance if the energy price rises or the climate conditions vary.

Theory

This section describes the theoretical building of the model used to predict effectiveness and pressure drop of the MEE. Most of it is based on previous work by the author [17]. For sensible and latent effectiveness, the ϵ -NTU method was used. The heat and moisture transfer mechanisms are described here across one membrane, first for empty channels, then for channels with spacers. For applications in MEE with several channels, the following equations can be applied by multiplying the transfer area of one membrane by the number of channels.

3.1 The ϵ -NTU method to predict effectiveness

The ϵ -NTU method is based on the following equation for the heat transfer rate and the effectiveness [29]:

$$q = \epsilon C_{min} \Delta T_{max} \quad (3.1)$$

Where q is the heat transfer rate [W]; ϵ is the effectiveness; C_{min} is the minimum between the heat capacity of the air at ambient temperature and the heat capacity of the air at outdoor temperature [J/K]; ΔT_{max} is the temperature difference between ambient air and outdoor air [K]. Consequently, $C_{min} \Delta T_{max}$ is the maximum thermodynamically possible heat transfer, that would be obtained in a perfect counter-flow heat exchanger of infinite length. q can be defined as:

$$q = U A \Delta T_m \quad (3.2)$$

Where U is the overall heat transfer coefficient across the membrane [W/(m².K)]; A is the transfer surface area [m²]; ΔT_m is the mean temperature difference over the whole surface of the heat exchanger [K]. The isobaric specific heat capacity of the air c_p is considered constant between -53,2°C and 26,9°C and equal to 1,006 kJ/(kg.K), as the variations within these temperatures are less than 0,09%.

With the assumption that $C_{min} = C_{max} = C_p$ we get [29]:

$$\epsilon = \frac{UA}{C_p} \frac{\Delta T_m}{\Delta T_{max}} \quad (3.3)$$

The number of transfer units (NTU) for heat transfer is defined as (3.4). Similarly a NTU for mass transfer (moisture) can be defined as (3.5) [38]:

$$NTU_s = \frac{U_s A}{C_p} = \frac{U_s A}{\dot{m} c_p} \quad (3.4)$$

$$NTU_l = \frac{\rho U_l A}{\dot{m}} \quad (3.5)$$

It can be shown that the effectiveness ϵ is a function of NTU and the heat capacity ratio C_{min}/C_{max} [14]. In our case, $C_{min}/C_{max} = 1$. There is no analytical relation between the NTU and the effectiveness for a quasi-counterflow exchanger in the literature, but Kays et al. (1968) established an solution providing the effectiveness as a function of the NTU in the cross-part and in the counter-part [13]:

Table 3.1: Effectiveness of the quasi-counterflow exchanger as function of the NTU in the counter- and cross- parts [13].

		NTU_{cross}							
		0	1	2	3	4	5	6	7
$NTU_{counter}$	0	0.000	0.476	0.615	0.682	0.723	0.752	0.773	0.790
	1	0.500	0.649	0.714	0.751	0.777	0.795	0.810	0.821
	2	0.667	0.739	0.775	0.798	0.815	0.828	0.838	0.846
	3	0.750	0.792	0.816	0.831	0.843	0.852	0.860	0.866
	4	0.800	0.828	0.844	0.855	0.863	0.870	0.876	0.880
	5	0.834	0.853	0.865	0.873	0.880	0.885	0.889	0.893
	6	0.856	0.872	0.881	0.887	0.892	0.897	0.900	0.903
	7	0.875	0.886	0.893	0.899	0.903	0.906	0.909	0.912

3.2 Sensible heat transfer coefficient U_s

The heat in the air is transferred to the membrane by convection, then crosses the membrane by conduction and finally it is transferred to the air on the other side by convection again. The transfer is driven by the temperature difference between the two sides of the membrane. The overall heat transfer coefficient, also called U-value of the membrane, in $W/m^2 K$, is defined as:

$$U_s = \left[\frac{1}{h_s} + \frac{\delta}{\lambda_m} + \frac{1}{h_e} \right]^{-1} \quad (3.6)$$

Where $h_{s/e}$ is the convective heat transfer coefficient [$W/(m^2.K)$] on the supply/exhaust side respectively; δ is the thickness of the membrane [m]; λ_m is the thermal conductivity

of the membrane $[W/(m.K)]$.

Since the membrane is very thin, the thermal resistance of the membrane can be neglected. Indeed, the thermal resistance of the membrane is calculated to account for 0,4-0,5% of the total thermal resistance. The convective heat transfer coefficients depend only on the flow configuration and the properties of air, which we assume to be the same on the supply and exhaust side (see Appendix H). Thus the coefficients h_s and h_e will be equal, and U_s can be expressed as:

$$U_s = \frac{h}{2} \quad (3.7)$$

3.2.1 Convective heat transfer coefficient h

The Nusselt number Nu is defined as:

$$Nu = \frac{hD_h}{\lambda_a} \quad (3.8)$$

Where D_h is the hydraulic diameter $[m]$; λ_a is the thermal conductivity of air $[W/(m.K)]$. The Nusselt number can be calculated from the aspect ratio α using the following correlation for a rectangular channel[29]:

$$Nu = 8.235(1 - 2.0421\alpha + 3.0853\alpha^2 - 2.4765\alpha^3 + 1.0578\alpha^4 - 0.1861\alpha^5) \quad (3.9)$$

The correlation is valid for laminar flow and under the hypothesis of constant axial heat flux and constant peripheral wall temperature, called $H1$ hypothesis. This hypothesis is not exactly verified for the quasi-counterflow exchanger, but it is an approximation of the actual conditions to get an estimation of the Nusselt number. The aspect ratio is defined as:

$$\alpha = \frac{height}{width} \quad (3.10)$$

With the Nusselt number we obtain the convective heat transfer coefficient by rearranging (3.8):

$$h = \frac{Nu\lambda_a}{D_h} \quad (3.11)$$

3.3 Moisture transfer coefficient U_l

In cold climate, the humidity will be higher in the exhaust air than in the supply air. The difference in partial pressure of the water vapor is the driving force behind the moisture transfer from one air stream to the other. The water vapor in the exhaust air stream will be transferred to the membrane by convection. It will then travel across the membrane by diffusion through the pores, and be transferred to the supply air stream by convection again. The moisture transfer coefficient U_l (m/s), similarly to U_s , is defined as:

$$U_l = \left[\frac{1}{k_s} + r_{mm} + \frac{1}{k_e} \right]^{-1} \quad (3.12)$$

Where $k_{s/e}$ is the convective moisture transfer coefficient between the surface of the membrane and the supply/exhaust air stream [m/s]; r_{mm} is the moisture diffusion resistance of the membrane [s/m]. As for h , the convective moisture transfer coefficients $k_{s/e}$ depend only on the flow configuration and the properties of air, so they will be equal for the supply and exhaust channel. However, unlike with heat transfer, the moisture transfer resistance of the membrane cannot be neglected. Indeed, it accounts here for 80% of the total resistance across the membrane for an empty channel. The following sections will show the calculations of k and r_{mm} for an empty channel.

3.3.1 Convective moisture transfer coefficient k for an empty channel

The convective moisture transfer coefficient can be obtained from the Sherwood number defined as:

$$Sh = \frac{kD_h}{D_v} \quad (3.13)$$

Where D_v is the diffusivity of water vapour in the air [m^2/s]. The Sherwood number represents the ratio of the convective mass transfer rate to the rate of diffusive mass transport. Rearranging the equation yields:

$$k = \frac{ShD_v}{D_h} \quad (3.14)$$

Sh can be determined using the Chilton-Colburn analogy. The Chilton-Colburn analogy is used here to calculate mass transfer coefficients when the heat transfer coefficients are known, taking advantage of the fact that the dimensionless equations governing heat and mass transfer are analogous [9]. In the Chilton-Colburn analogy, this translates into:

$$j_H = StPr^{2/3} = \frac{Nu}{RePr^{1/3}} \quad 0.6 < Pr < 60 \quad (3.15)$$

$$j_m = St_mSc^{2/3} = \frac{Sh}{ReSc^{1/3}} \quad 0.6 < Sc < 3000 \quad (3.16)$$

And

$$j_H = j_m \quad (3.17)$$

Where St , St_m are the Stanton and mass Stanton numbers, and Re , Pr and Sc are the Reynolds, Prandlt and Schmidt numbers respectively, defined as:

$$Re = \frac{uD_h}{\nu} \quad Pr = \frac{c_p\mu}{\lambda_a} \quad Sc = \frac{\nu}{D_v} \quad (3.18)$$

With u the velocity of the fluid [m/s]; ν the kinetic viscosity [m^2/s]; μ the dynamic viscosity [$kg/(m.s)$ or $Pa.s$].

Using the Chilton-Colburn analogy, the Sherwood number can be written as:

$$Sh = Nu \left(\frac{Sc}{Pr} \right)^{1/3} \quad (3.19)$$

$$Sh = NuLe^{1/3} \quad (3.20)$$

Where Le is the Lewis number, which represents the ratio of thermal diffusivity to mass diffusivity, defined as $Le = Sc/Pr$. The analogy is valid for laminar flow if $dp/dx < 0$ [9], i.e. if the pressure is reduced as we progress in the direction of the flow, which is the case for the fully developed flow. The configuration of this exchanger gives $Pr = 0.73$ and $Sc = 0,64$, thus $Le = 0.86$; thus, the analogy is valid. Using (3.20) to replace Sh in (3.14), we get:

$$k = \frac{NuLe^{1/3}D_v}{D_h} \quad (3.21)$$

3.3.2 Moisture diffusion resistance of the membrane r_{mm}

Membranes are usually divided into two categories: dense membranes and porous membranes. Both types of membranes have pores, but the size of the pores is different. For dense membranes, the pore size is in the order of 1 nm , and for porous membranes the pore size is in the order of $1\text{ }\mu\text{m}$ [18]. As a result, the moisture transfer mechanisms through dense and porous membranes have to be described differently. In the MEE studied in this project, the membrane used is of porous type. For simplification it is assumed that the membrane pores are all the same size and perpendicular to the membrane. Thus, the Hagen-Poiseuille equation may be used to describe water vapor flow through the membrane [23]:

$$J = \frac{\epsilon r^2}{8\eta\tau} \frac{\Delta P_v}{\delta} \quad (3.22)$$

Where J is the volume flux [$m^3/(m^2.s)$] of water vapor through the membrane ; ϵ is the porosity [%], defined as the ratio of pore surface to membrane surface; r is the pore radius [m]; η is the viscosity of the air [$Pa.s$]; τ is the tortuosity ($\tau = 1$ for cylindrical perpendicular pores); ΔP_v is the water vapor partial pressure difference [Pa] from one side of the membrane to the other; δ is the thickness of the membrane [m].

$\epsilon r^2/8\eta\tau$ is defined as the diffusivity of the membrane D_p . It has been measured by the manufacturer using a water vapour transfer test. The water vapour transfer is $8.4\text{ kg}/(m^2/day)$ at 25°C isothermal conditions, with one stream at 50% RH and the other stream at 0% RH. The calculation of the water vapor diffusivity of the membrane from the water vapor transfer test can be found in Appendix B. The moisture diffusivity of the membrane is assumed constant under different vapour pressures, because the membrane is assumed to be isoporous and hydrophobic [22]. Thus, if the pores all have the same size, all the pores can transfer moisture the same way under the same vapor pressure conditions.

Rearranging the definition of relative humidity RH, an expression for P_v can be obtained:

$$RH = \frac{P_v}{P_{sat}} \quad (3.23)$$

$$P_v = P_{sat}.RH \quad (3.24)$$

The relation between RH [%] and the moisture content w [kg/kg] is [22]:

$$\frac{RH}{w} = \frac{P}{0,622P_{sat}} - \frac{RH}{0,622} \quad (3.25)$$

In cold climate, the term $RH/0,622$ can be neglected because the water vapour pressure P_v [$RH = P_v/P_{sat}$] is much lower than the atmospheric pressure P [22]. Rearranging (3.25), we get:

$$RH.P_{sat} = \frac{P.w}{0,622} \quad (3.26)$$

By replacing (3.26) in (3.24), and introducing a standard atmospheric pressure of 101325 Pa, is obtained:

$$P_v = 1.63 \times 10^5 w \quad (3.27)$$

Thus the Hagen-Poiseuille equation (3.22) can be rewritten as:

$$J = 1.63 \times 10^5 D_p \frac{\Delta w}{\delta} \quad (3.28)$$

The moisture transfer diffusive resistance is defined as [22]:

$$r_{mm} = \frac{\Delta w}{J} \quad (3.29)$$

Using (3.28) to replace J in (3.29):

$$r_{mm} = \frac{\delta}{1.63 \times 10^5 D_p} \quad (3.30)$$

3.4 Pressure drop

The total pressure drop of a channel of the quasi-counterflow exchanger is composed of several contributions:

1. The pressure drop due to entrance effects
2. The core pressure drop in the cross part
3. The pressure drop due to bends in the flow path
4. The core pressure drop in the counter part
5. The pressure drop/rise due to exit effects

With air temperature changes, the air density also changes. However those variations are small in the range of temperatures that is considered, so the density is assumed constant. Consequently, pressure drop due to momentum change from variations in density is not taken into account.

Pressure drop calculations are different for different flow regimes. In this thesis and in accordance with experimental results, the flow is assumed to be always laminar.

3.4.1 Core pressure drop for the fully developed flow in the cross- and counter-parts

The pressure losses due to friction in the cross- and the counter- parts, also called major losses, are the largest contribution to total pressure drop. To calculate them, a simplification of the flow pattern is made. The stream lines are assumed to be straight and perpendicular to the entrance/exit of the cross-parts, and straight and parallel to the overall direction of the flow in the counter-part. The angle at each end of the cross-parts being 90°, the two cross-parts are like two halves of a square. Thus the exchanger core can be virtually cut and rearranged as a rectangle part and a square part with straight flows in both (fig.3.1). The two parts have different cross-sectional areas resulting in different velocities, aspect ratios and hydraulic diameters. The pressure losses due to bends will be calculated separately.

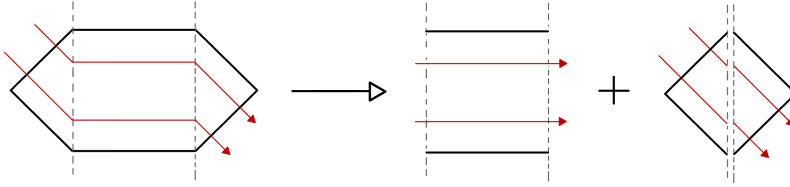


Figure 3.1: Simplification of the flow pattern

The pressure drop for a flow in a rectangular channel is [29]:

$$\Delta p = f \frac{LG^2}{2\rho g_c D_h} \quad (3.31)$$

Where f is the Darcy friction factor; L is the length of the channel; G is the specific mass flow rate [$kg/(m^2 \cdot s)$]; ρ is the density of air [kg/m^3]; g_c is the proportionality constant in Newton's second law of motion ($g_c = 1$ in SI units); D_h is the hydraulic diameter of the channel [m].

The product $f \cdot Re$ is a constant for laminar fully developed flow that depends on the geometry of the channel. For an empty rectangular channel, a correlation for $f_F \cdot Re$ and the aspect ratio α can be found in [29]:

$$f_F \cdot Re = 24(1 - 1,3553\alpha + 1,9467\alpha^2 - 1,7012\alpha^3 + 0,9564\alpha^4 - 0,2537\alpha^5) = cst \quad (3.32)$$

Where f_F is the Fanning friction factor. The relation between the Fanning friction factor and the Darcy friction factor is:

$$f = 4f_F \quad (3.33)$$

From there the Darcy friction factor can be calculated as:

$$f = \frac{4 \cdot cst}{Re} \quad (3.34)$$

The major loss for both the cross- and counter-part is:

$$\Delta p_{major} = \frac{f_{cross} L_{cross} G_{cross}^2}{2\rho g_c D_{h,cross}} + \frac{f_{counter} L_{counter} G_{counter}^2}{2\rho g_c D_{h,counter}} \quad (3.35)$$

3.4.2 Entrance and exit pressure drop

When the flow enters a channel of the MEE, the cross-sectional area is reduced and the flow is subjected to a sudden contraction which is followed by a free expansion (see fig. 3.2). When the flow exits the channel, the cross-sectional area is increased and the flow is subjected to a free expansion. In each case two effects come into play:

1. The decrease of cross-sectional area causes a pressure drop while the increase of cross-sectional area causes a pressure rise.
2. The irreversible free expansion, preceded or not by a sudden contraction, causes a pressure loss.

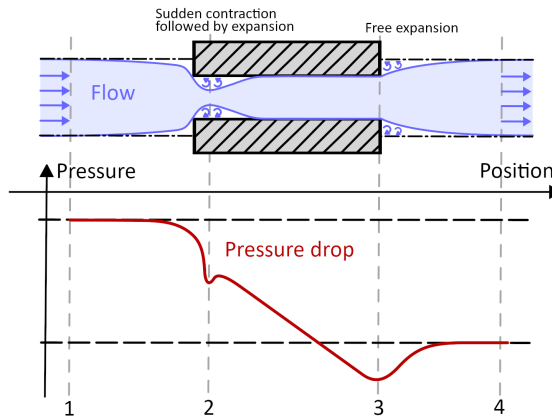


Figure 3.2: Pressure profile for an air stream entering and exiting a channel.

The pressure drop/rise due to cross-sectional area change can be explained by the Bernoulli equation. It is accounted for by the term $(1 - \sigma^2)$ where σ is the ratio of channel cross-sectional area to frontal area at the entrance/exit ($\sigma < 1$) [29].

$$\sigma = \frac{A_2}{A_1} = \frac{A_3}{A_4} \quad (3.36)$$

Where the subscript numbers refer to the position on figure 3.2 and A is the cross-sectional free-flow area. As the membrane is very thin and the supply and exhaust channels have equal spacing, we have $\sigma = 0.5$. The pressure drop for free expansion is accounted for by the expansion coefficient K_e . The pressure drop for sudden contraction followed by free expansion is accounted for by the contraction coefficient K_c . Values of K_e and K_c can be found for different channel geometries in Shah et al. (2003), and the values of interest are reported in table 3.4 [29].

Finally, the pressure drops due to entrance and exit effects are calculated as:

$$\Delta p_{entrance} = [(1 - \sigma^2) + K_c] \frac{G^2}{2g_c\rho} \quad (3.37)$$

$$\Delta p_{exit} = [(\sigma^2 - 1) + K_e] \frac{G^2}{2g_c\rho} \quad (3.38)$$

$$(3.39)$$

3.4.3 Pressure drop due to bends

As we can see in figure 3.1, there are two 45°bends in one stream line. These bends will cause an additional pressure drop. Pressure drop numbers $K_{L,bend}$ for different angles and different aspect ratios are given by ASHRAE [1]. As the aspect ratio in the counter part is outside the given range, a polynomial interpolation has been used to extrapolate the values (fig.3.3).

The pressure loss due to a bend is:

$$\Delta p_{bend} = K_{L,bend} \frac{G^2}{2g_c\rho} \quad (3.40)$$

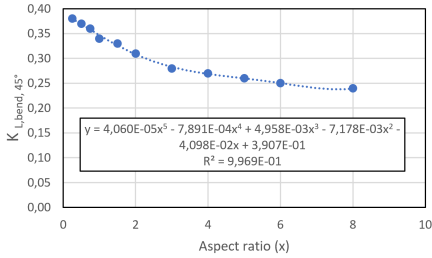


Figure 3.3: Correlation between $K_{L,bend}$ and aspect ratio α for a 45°bend

Minor losses	Symbol	Value
Entrance, parallel plates	K_c	0.713
Entrance, triangular fins	K_c	1.175
Exit, parallel plates	K_e	0.063
Exit, triangular fins	K_e	-0.175
45°bend	$K_{L,bend}$	0,3904

Figure 3.4: Pressure drop numbers used in the calculations for $\sigma = 0.5$ [29, 1].

3.4.4 Total pressure drop

The total pressure drop for a channel is the sum of the major losses due to friction and the minor losses due to entrance and bends effects.

$$\Delta p_{tot} = \Delta p_{major} + \Delta p_{entrance} + 2\Delta p_{bend} + \Delta p_{exit} \quad (3.41)$$

3.5 Channel with spacer

3.5.1 Heat and mass transfer

When there is heat or mass transfer between the air and the surface of the membrane, the major temperature or concentration changes occur in the thin layer of air close to the surface of the membrane. It can be referred to as *fluid film near the surface* or *boundary layer* [29]. The heat/mass boundary layer is not the same as the velocity boundary layer, which is formed by viscosity effects close to the surface. Boundary layers start to form at the entrance of the channel. They are very thin at the entrance and become larger along the flow (fig. 3.5). They can be understood as heat/moisture transfer resistances and are characterized by the convective transfer coefficients h and k :

$$h = \frac{\lambda_a}{\delta_{bh}} \quad k = \frac{D_v}{\delta_{bm}} \quad (3.42)$$

Where δ_{bh} and δ_{bm} are the thickness of the temperature boundary layer and mass boundary layer respectively. It follows that the smaller the boundary layers are, the larger are the Nusselt and Sherwood number and the larger are the heat and moisture transfer [zhang'chapter'2013].

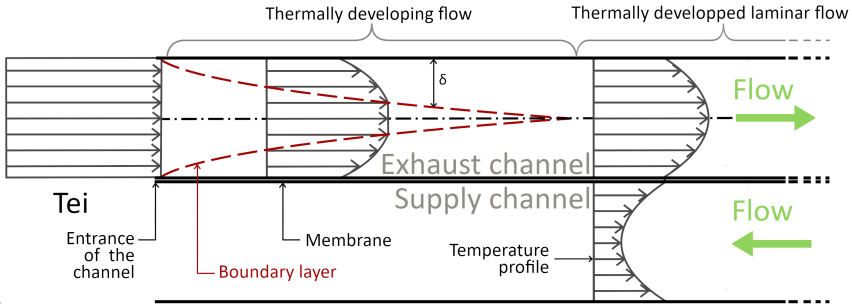


Figure 3.5: Temperature boundary layer build-up in laminar flow.

The presence of a spacer in the channel can improve heat and mass transfer as the wires of the spacer interrupt the formation of the boundary layer. It results in thinner boundary layers along the flow and thus higher Nu and Sh [16].

As the calculation of boundary layer thickness is beyond the scope of this thesis, to predict effectiveness of a MEE with spacers, the Colburn factor has to be known. It can be obtained with correlations from previous studies if available, or measured experimentally, as it is the case here (see p.31). When the Colburn j factor is known, using (3.15) and (3.18) to rearrange (3.11), and using (3.16) and (3.18) to rearrange (3.21) we get:

$$h = j_h \frac{c_p \rho u}{Pr^{2/3}} \quad k = j_m \frac{\rho u (\nu D_v)^{2/3}}{\mu} \quad (3.43)$$

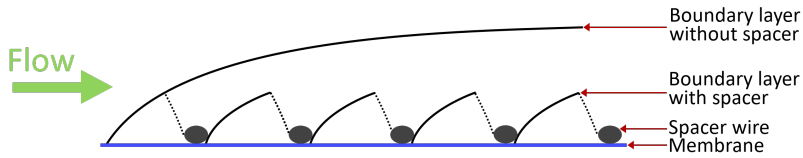


Figure 3.6: Boundary layer with and without spacer.

Then, the calculations of sensible and latent effectiveness are done as for an empty channel.

3.5.2 Pressure drop

With a spacer inside the channel, the pressure drop is necessarily higher. This can be modelled with a higher friction factor which is found experimentally. Additionally, the friction factor can be different in the cross- and in the counter-part, not only because the velocity is different but also because the orientation of spacer corrugation may not be the same. For example, for a corrugated mesh spacer as in fig.3.7, the flow is angled with regards to the corrugation in the cross-part, while in the counter-part the flow is parallel to the corrugation. As a consequence, the friction factor is higher in the cross-parts than in the counter-part. Woods et al. (2013) found a friction factor in average 80% higher for a spacer with corrugation angled 45° to the flow direction than for a spacer with parallel corrugation [35].



Figure 3.7: Flow direction through the spacer.

Measurements

4.1 Test rig

Measurements were conducted on the membrane energy exchanger test rig of NTNU's Energy and Process Engineering lab. The rig consists of a MEE core connected with insulated ducts to a refrigeration room to simulate outdoor conditions (fig. 4.1). Four manually controlled fans, one in each duct, deliver the driving force. Two orifice plates with pressure taps are used to measure flow rate on the supply and exhaust side. Four thermocouples are placed with regular spacing in each of the MEE's inlets/outlets, which are also equipped with relative humidity sensors and pressure taps. At the entrance of the extract air duct is installed a water spray nozzle to control the humidity of exhaust air. The thermocouples, humidity sensors and spray nozzle are monitored with a pre-existing LabView™ program. The manometers were monitored manually.

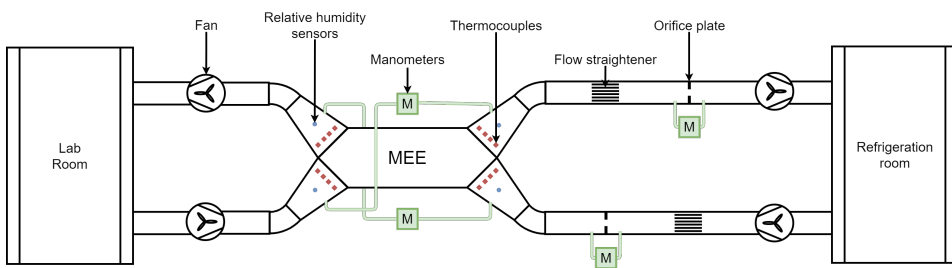


Figure 4.1: Schematic of the test rig.

The MEE core has 9 channels on each side of the flow, 18 in total. The structure is made of plastic plates on top and bottom, and plastic brackets on the sides, sealed with glue. The plastic brackets are placed in between the membrane layers to create 2mm high air channels (fig. 4.2). Spacers were made of aluminium mesh that was corrugated using a lab-fabricated mould. Dimensions of the exchanger and spacers are given in figure 4.3.

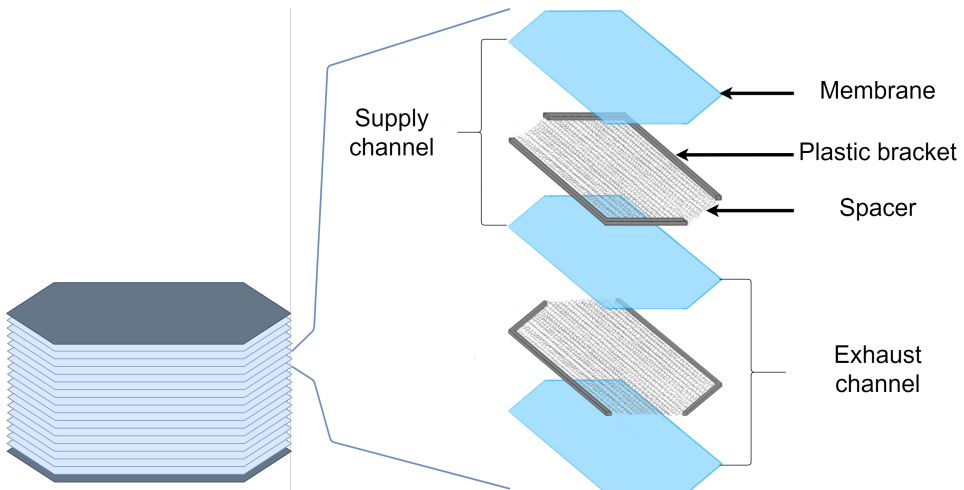


Figure 4.2: Split view of the exchanger core.

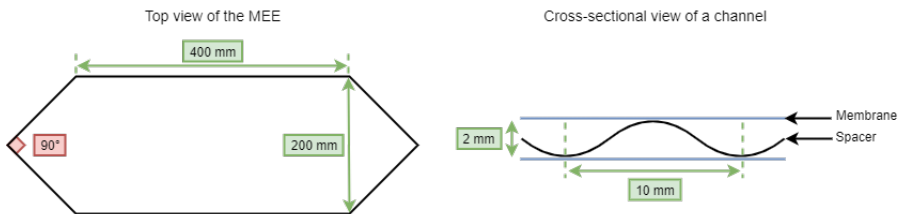


Figure 4.3: Dimensions of the exchanger core.

4.2 Measurements devices

4.2.1 Thermocouples and relative humidity sensors

The temperature at inlets and outlets is measured by 16 T-type thermocouples fabricated in the lab and calibrated between -20°C and 20°C using a PettersenTM T-type thermocouple, with accuracy of $\pm 0.05^{\circ}\text{C}$ [18].

The relative humidity at inlets and outlets is measured by VaisalaTM humidity and temperature transmitters (HMT330). Their accuracy is $\pm 0.8\%$ of reading $\pm 1.0\%$ RH (between -20°C and $+40^{\circ}\text{C}$) for relative humidity; and $\pm 0.2^{\circ}\text{C}$ at 20°C for temperature.

4.2.2 Manometers

To measure the pressure drop across the exchanger on the supply side and on the exhaust side, two micro-manometers (DP0, DP1) were connected to the pressure taps. The micro-manometers model TT470S are manufactured by DPM and their uncertainty $\pm 1\%$ of reading $\pm 0,1$ Pa. Two manometers CP101 manufactured by KIMO[®] (DP2, DP3) were

connected the pressure taps of the orifice plates to measure flowrate. Their uncertainty is $\pm 1,5\%$ of reading ± 3 Pa.

It was noticed that the manometers were not measuring the same value for the same differential pressure. The differential pressure was thus measured across the orifice plate on the supply side with all the manometers successively, and at different flow rates. Correlations were then established between the measurements of one reference manometer and the three others. The manometer labeled DP0 was chosen as the reference since it was a micromanometer, thus more precise than the two CP101, and the most recently calibrated one. The correlations were found to be linear and using a the MATLAB polyfit function for a first degree polynomial we find:

$$DP1 = -2.1978 + 1.1017 \cdot DP0 \quad (4.1)$$

$$DP2 = +1.4885 + 1.0134 \cdot DP0 \quad (4.2)$$

$$DP3 = -1.3982 + 1.0145 \cdot DP0 \quad (4.3)$$

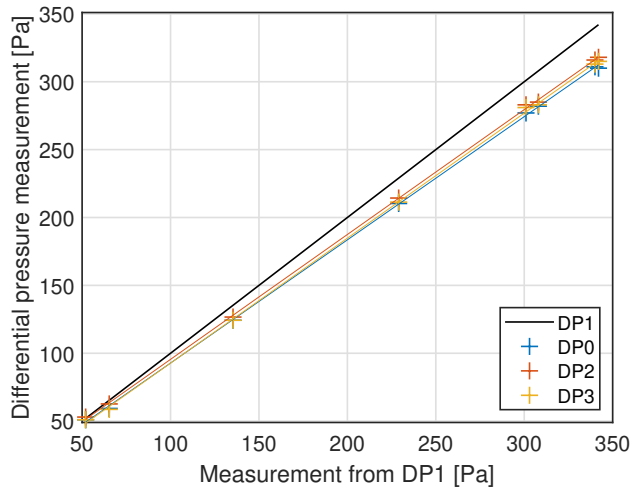


Figure 4.4: Manometer correlations

Table 4.1: Measurement devices.

Device	Manufacturer	Uncertainty
Thermocouples	Lab	$\pm 0.05^\circ\text{C}$
Relative humidity sensor HMT330	Vaisala	$\pm 0.8\%$ of reading $\pm 1.0\%$ RH $\pm 0.2^\circ\text{C}$
Manometers CP101	KIMO	$\pm 1,5\%$ of reading ± 3 Pa
Micro-manometers TT470S	DPM	$\pm 1\%$ of reading $\pm 0,1$ Pa

4.3 Measurement of flow with orifice plates

The air flow rate was measured using orifice plates inserted in the ducts (fig.4.1). The orifice plates are metal discs with a central hole. Pressure taps are installed on each side of the orifice plate and connected to a manometer to measure the pressure drop across the plate. From the pressure drop the flow rate is calculated iteratively according to the method described in standard ISO 5167-2. A pre-existing Excel sheet created by Hans Martin Mathisen was used to perform the calculation. The parameters used in the calculation are documented in table 4.2. Four different flow rates were used for each measurement case, the correspondence between pressure drop across the orifice plate and the calculated air flow rate is given in table 4.3.

Table 4.2: Parameters used in orifice plate air flow rate calculation.

Parameter	Value
Diameter of orifice [mm]	45
Diameter of duct [mm]	100
Dynamic viscosity of air [Pa.s] at 293 K	1,83E-05
Kinematic viscosity of air [m ² /s] 293 K	1,525E-05
Density of air ρ [kg/m ³]	1,2
Diameter ratio β	0,45
Discharge coefficient	0,6061

Table 4.3: Pressure drop measurement across orifice plate and calculated air flow rate.

Pressure drop [Pa]	Volume flow rate [L/s]
4	2,54
7	3,36
11	4,21
14	4,75

4.4 Data acquisition and treatment

Sensible and latent effectiveness have been measured at 2.5 L/s, 3.4 L/s, 4.2 L/s and 4.7 L/s in 4 different cases:

- Case 025: $T_{out} = 0^\circ\text{C}$ and $RH_{out} = 26\% \pm 1\%$
- Case 030: $T_{out} = 0^\circ\text{C}$ and $RH_{out} = 30\% \pm 5\%$
- Case 040: $T_{out} = 0^\circ\text{C}$ and $RH_{out} = 43\% \pm 5\%$
- Case 530: $T_{out} = 5^\circ\text{C}$ and $RH_{out} = 34\% \pm 2\%$

The cold chamber was turned on the day before the measurements to reach set point temperature during the night. The fans were turned on and balanced one hour before the data acquisition, so that the system reaches steady state. When changing the flowrate, a delay of 10-15 minutes was needed to reach steady state again. If the humidifier was needed, it was turned on a few minutes before starting the acquisition. Humidity had an on/off type of control through LabView, with open-loop frequency control. Consequently, the relative humidity could not be controlled with precision, and a relatively high variability can be observed in Case 030 and Case 040. The exhaust inlet relative humidity data labels are displayed on the corresponding figures (fig.4.5b and fig.4.6a). For each case, temperatures and relative humidity were acquired for 20 minutes, with a sampling period of 1 minute. While the data was logging, the pressure drop values were noted manually every 4 minutes. The data was saved in Excel format to be later treated in MATLAB.

4.4.1 Effectiveness and Colburn factor

When the heat capacities are equal on both sides of the exchanger, the sensible effectiveness and the temperature efficiency are equal. The sensible and latent effectiveness are calculated as:

$$\epsilon_s = \frac{T_{so} - T_{si}}{T_{ei} - T_{si}} \quad \epsilon_l = \frac{w_{so} - w_{si}}{w_{ei} - w_{si}} \quad (4.4)$$

Where T_{so} is the outlet supply temperature; T_{si} is the inlet supply temperature; and T_{ei} is the inlet exhaust temperature. With the same corresponding subscripts, w_* is the moisture content of air, calculated from RH as (see p.17):

$$w = \frac{RH \cdot 10^7}{6.462 \exp\left(\frac{5419}{T}\right)} \quad (4.5)$$

The measurement results are shown on figure 4.5 and figure 4.6. They are used to calculate a Colburn factor correlation for the lab MEE. The Colburn factor is calculated by inverting the solution from Kays (table 3.1) to get NTU_x and NTU_c from the sensible effectiveness. The MATLAB function KaysEff has been created to interpolate and extrapolate the values from table 3.1 (see Appendix C).

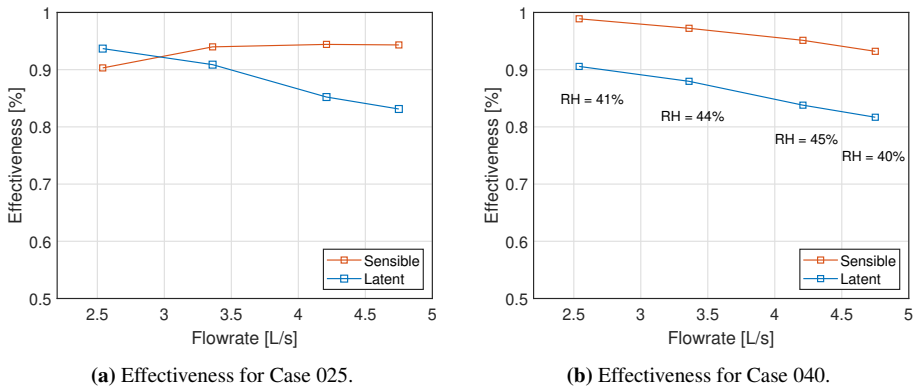


Figure 4.5: Measured effectiveness for Case 025 and Case 040.

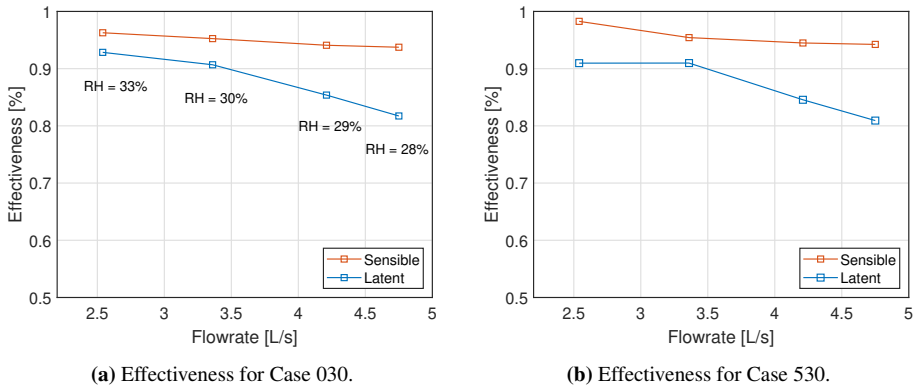


Figure 4.6: Measured effectiveness for Case 030 and Case 530.

To be able to invert the KaysEff function, and find a single solution, a hypothesis on the NTU has to be made. The hypothesis that was chosen is to consider that the heat transfer is the same in the cross- and in the counter-part, and so that:

$$\frac{NTU_x}{A_x} = \frac{NTU_c}{A_c} \quad (4.6)$$

And thus:

$$\frac{NTU_x}{NTU_c} = \frac{A_x}{A_c} \quad (4.7)$$

This additional equation removes one degree of freedom so that a single $NTU_{tot} = NTU_x + NTU_c$ can be found for one value of effectiveness (fig. 4.7). This has been done in a second MATLAB function e2NTU, using a Newton method (see Appendix D).

When the number of transfer units is obtained, the overall Colburn factor is:

$$j = \frac{2\dot{m}Pr^{2/3}NTU_{tot}}{\rho u_c A_{tot}} \quad (4.8)$$

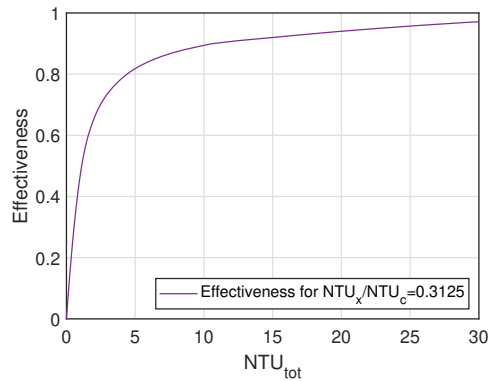


Figure 4.7: Effectiveness for the total NTU, with $NTU_x/NTU_c = 0.3125$

The Colburn factor for the different flowrates is then plotted against the Reynolds number and fitted with a power law. The correlation is made from the average of Colburn factors from Case 030, Case 040 and Case 530. Case 025 has not been used to establish the correlations because there is an outlier data point for 2.5 L/s that is suspected to be due to errors in the measurement process. The correlation found is:

$$j = 8.44Re^{-0.87} \quad R^2 = 0.999 \quad (4.9)$$

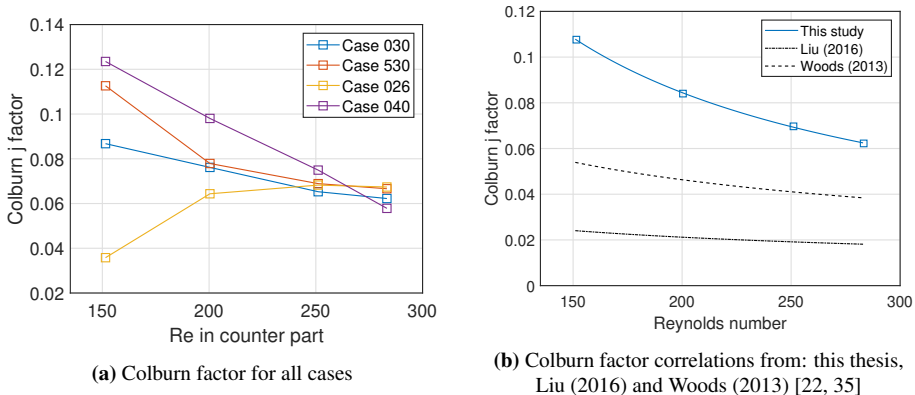


Figure 4.8: Experimental Colburn factor

4.4.2 Pressure drop and friction factor

The pressure drop was measured on the exhaust side and on the supply side using the micromanometers for the 4 flowrates in each case. Before starting a measurement series, the flowrate was adjusted by measuring the pressure drop across the orifice plates to obtain the desired flow. The fans on each side of the exchanger were balanced by adjusting fan

speeds until the pressure drop is equal on the supply and exhaust side, while keeping the desired flowrate. If the fans are not properly balanced, the pressure drop in the MEE and the flowrate show anomalous values. This can be attributed to the fact that if there is overpressure or underpressure on the supply or exhaust side, the membrane is likely to be deflected and thus the flow will be partially obstructed on the underpressured side.

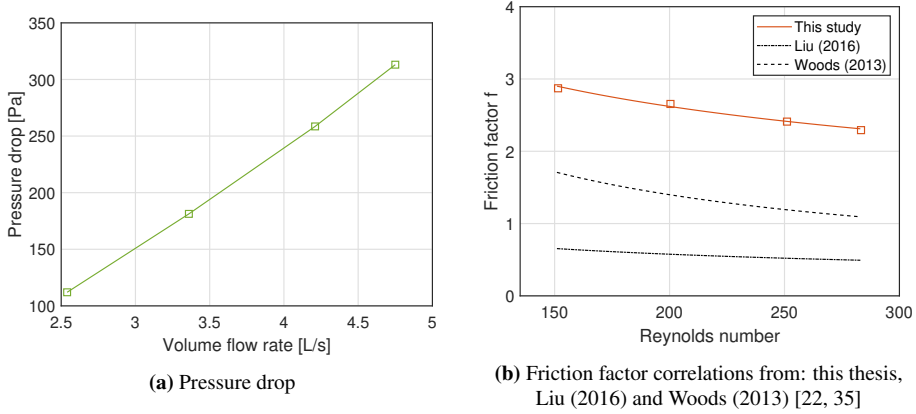


Figure 4.9: Experimental Darcy friction factor

When the fans are balanced, the pressure drop is the same on the supply and exhaust side. The pressure drop on each side has been noted manually throughout the data acquisition for each case. A total of 30 pressure drop measurements have been averaged for each flowrate. Then, the friction factor has been calculated and a correlation as been drawn and compared to previous studies (fig.4.9b). The Darcy friction factor is calculated as follows:

$$\Delta P_{major} = \Delta P - 2\Delta P_{bend} - \Delta P_{entrance} - \Delta P_{exit} \quad (4.10)$$

$$f_{exp} = \frac{2D_h \Delta P_{major}}{\rho u_c^2 L_{tot}} \quad (4.11)$$

The correlation found with a power law fit is:

$$f = 17.84 Re^{-0.362} \quad R^2 = 0.989 \quad (4.12)$$

4.5 Uncertainty analysis

Three main categories of errors can be identified [31]:

- U_G Gross errors are often due to the operator's lack of attention and must be avoided. Here, we assume $U_G=0$.
- U_S Systematic errors can be the error from the measuring device or a methodical error from the operator. For calculations, we assume that U_S is equal to the error from the device.

- U_T Accidental errors can be caused by poor resolution of the measuring device or external interference. These errors cannot be avoided but can be reduced if the measurement is repeated many times.

The systematic error U_S is given by the manufacturer of the device. The accidental error U_T when the measurement is repeated n times, with a standard deviation of σ is:

$$U_T = \pm \frac{\sigma}{\sqrt{n}} \quad (4.13)$$

When U_S and U_T are known, the resulting uncertainty is:

$$\Delta u = \sqrt{U_S^2 + U_T^2} \quad (4.14)$$

4.5.1 Temperature and moisture content

Relative humidity is a simple (direct) measurement: the relative humidity is obtained directly from the transmitter. Thus, the uncertainty for a relative humidity measurement repeated n times is:

$$U_{S,RH} = \pm(1.0 + 0.008 * reading)\%RH \quad (4.15)$$

$$U_{T,RH} = \pm \frac{\sigma}{\sqrt{n}} \quad (4.16)$$

$$\Delta RH = \pm \sqrt{U_{S,RH}^2 + U_{T,RH}^2} \quad (4.17)$$

Pressure drop is also a simple measurement and the uncertainty for pressure drop is calculated the same way. Moisture content of air, however, is a complex measurement. It is calculated from relative humidity as in equation (4.5), and is also dependent on the air temperature. As the uncertainty of the relative humidity measurement and the uncertainty of the temperature measurement are independent, the moisture content uncertainty can be calculated as (with T in Kelvins):

$$\Delta w = \pm \sqrt{\left(\frac{\partial w}{\partial RH} \Delta RH\right)^2 + \left(\frac{\partial w}{\partial T} \Delta T\right)^2} \quad (4.18)$$

$$\Delta w = \pm \sqrt{\left(\frac{\Delta RH \cdot 10^7}{6.462 \exp(5419/T)}\right)^2 + \left(\frac{5418}{T^2} w \Delta T\right)^2} \quad (4.19)$$

Temperature is a simple measurement: the temperature is obtained directly from the thermocouple. However, the temperature at each inlet and outlet of the MEE is the average of the temperatures given by four thermocouples, so it is a complex measurement. Since the average temperature is composed of linearly independent variables, the formula used in equation (4.19) can be simplified to:

$$T_* = \frac{T_1 + T_2 + T_3 + T_4}{4} \quad (4.20)$$

$$\Delta T_* = \pm \frac{1}{4} \sqrt{(\Delta T_1)^2 + (\Delta T_2)^2 + (\Delta T_3)^2 + (\Delta T_4)^2} \quad (4.21)$$

4.5.2 Sensible and latent effectiveness

The sensible effectiveness is a compound measurement that uses three composite temperature measurements as in eq. 4.21:

$$\epsilon_s = \frac{T_{so} - T_{si}}{T_{ei} - T_{si}} \quad (4.22)$$

The equation for variables that are not linearly independent is to be used:

$$\Delta\epsilon_s = \pm\sqrt{\left(\frac{\partial\epsilon_s}{\partial T_{so}} \Delta T_{so}\right)^2 + \left(\frac{\partial\epsilon_s}{\partial T_{ei}} \Delta T_{ei}\right)^2 + \left(\frac{\partial\epsilon_s}{\partial T_{si}} \Delta T_{si}\right)^2} \quad (4.23)$$

$$\Delta\epsilon_s = \pm\sqrt{\left(\frac{\Delta T_{so}}{T_{ei} - T_{si}}\right)^2 + \left(\frac{T_{si} - T_{so}}{(T_{ei} - T_{si})^2} \Delta T_{ei}\right)^2 + \left(\frac{T_{so} - T_{ei}}{(T_{ei} - T_{si})^2} \Delta T_{si}\right)^2} \quad (4.24)$$

The same calculation is used for latent effectiveness.

4.5.3 Resulting uncertainties

The uncertainties for one data point are given as an example in table 4.4. All the measurement data with the corresponding uncertainties are presented in Appendices I, J, K and L.

Uncertainties are large for latent effectiveness compared to sensible effectiveness. On the one hand, the mean uncertainty for latent effectiveness is 8% and is representative of all the measurements. It is mostly due to the error from the sensor. As this error cannot be reduced, one way to reduce the uncertainty is to repeat the same measurement more times, or to have a longer acquisition time. Another way is to have a better control of exhaust relative humidity to reduce the variability in the measurements. On the other hand, the uncertainty for sensible effectiveness is much more variable and ranges between 0.3% and 2.0% of effectiveness. For pressure drop, although there is a lot of variability in the measurements, it is compensated by the large number of these measurements, so that the uncertainty is reduced.

Table 4.4: Uncertainties for Case 030 at 3.4 L/s.

Measurement	Uncertainty
Air temperature T_{so}	$\pm 0.047^\circ\text{C}$ @ 21.25°C
Relative humidity RH_{so}	$\pm 1.3\%\text{RH}$ @ $29.0\%\text{RH}$
Sensible effectiveness	$\pm 0.1\%$ @ 95.2%
Latent effectiveness	$\pm 8.3\%$ @ 90.7%
Pressure drop	$\pm 3.3\text{Pa}$ @ 181.3Pa

4.6 Propositions for new spacers

A new prototype of spacer has been created in the lab. The fabrication process will be described here for potential use in further work. Spacers fabricated in the lab and currently in use in the MEE have a straight corrugation. These spacers are fabricated using aluminium mesh screen that are pressed between corrugated moulds, then cut into the shape of the MEE. In the cross-flow headers, the direction of the flow is not parallel to the corrugation, resulting in a higher pressure drop.

The idea is to create a spacer which follows more or less the flow patterns so as to reduce pressure drop. Previous attempts were made to make such a spacer using moulds with an angled corrugation at the location of headers. However the attempts were not successful as the mould was causing the mesh to rupture. The proposed fabrication process uses the same moulds with straight corrugation, and takes advantage of the flexibility of the mesh to create the wavy shape.

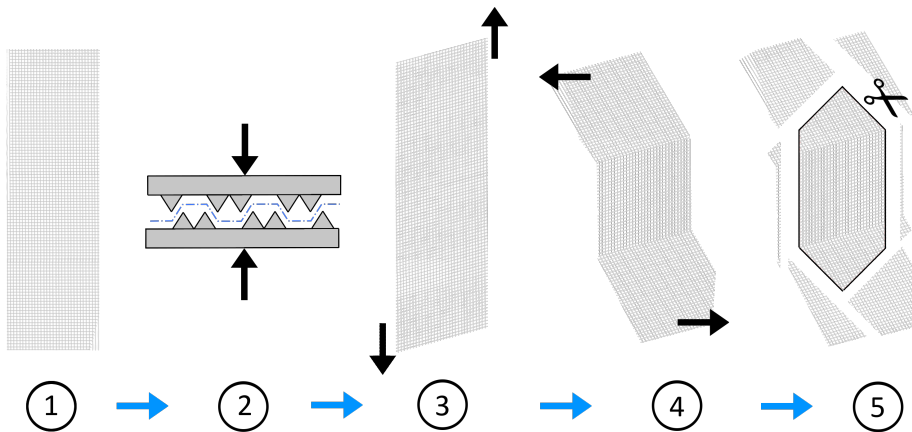


Figure 4.10: Fabrication steps

The following steps describe what was done to create the prototype:

1. Press the mesh inside the mould.
2. Deform the mesh so that vertical wires stay vertical and horizontal wires are angled 22.5° to the original horizontal axis.
3. Where the cross-flow headers should be, bend the mesh sideways to 45° to the vertical axis.
4. Cut the mesh into the shape of the MEE.

Advantages of this spacer are:

- Possible reduction of pressure drop, due to a corrugation being closer to the flow patterns that form when the channel is empty.
- Flexibility of shape: The corrugated mesh can be bent easily to different angles as long as they are not too sharp.
- Possibility to use the same mould for different shapes.

Disadvantages of this spacer are:

- Possible lack of precision when bending the mesh by hand, to make identical spacers.
- When the mesh is deformed, the corrugation size is reduced as well as the porosity of the mesh. A possible way to keep a constant corrugation size would be to perform step 2 of the fabrication process before step 1. However the porosity will be reduced no matter what, which is a factor that increases pressure drop. Large mesh size should be used.
- This shape of spacer would be perfectly fitted to an MEE with equilateral triangle headers. Indeed, if the entrance of the cross-part and the entrance of the counter-part are to have the same number of corrugations of the same size, then they should be of the same width. In our case, with square-angled headers, the flow lines will have to somewhat deviate from the spacer pattern.

Model

5.1 Description of the modelled installation

Based on the measurements performed on the lab exchanger, a ϵ -NTU and pressure drop model of a 36-channel membrane energy exchanger was coded in MATLAB (see Appendix F). The purpose of this model is to calculate the annual energy savings permitted by the exchanger in a virtual 45 m^2 house and compare the performances of the exchanger with different spacers. The influence of different parameters like channel spacing and shape of the MEE has been analysed.

The ventilation system is sized for a small single floor house with 45 m^2 floor surface. The ventilation rate is assumed constant and calculated on the basis of 0.5 air changes per hour with a 2.5 m high ceiling. The ventilation rate is thus 15,6 L/s, consequently the exchanger in the model will have 36 channels on each side of the flow, 72 in total. The energy savings have been calculated for the yearly weather conditions of Trondheim, Bergen and Oslo.

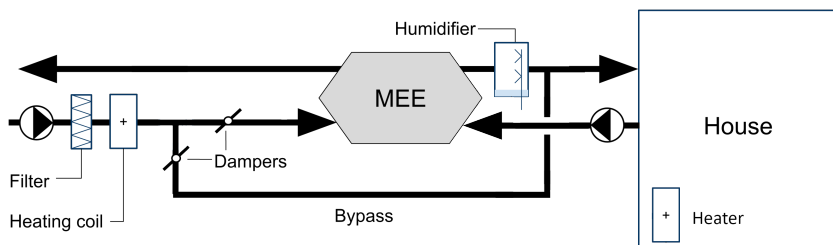


Figure 5.1: Schematic of the installation

The HVAC system comprises on the supply side a filter, a pre-heating coil to avoid frost formation and a humidifier, in series with the MEE (fig. 5.1). These elements add an additional pressure drop in the system, which is assumed to be 60 Pa. The pressure drop due to the ducts is negligible as the ducts are assumed to be short for a small house. Commonly in Norway, there is no cooling or dehumidifying system. Instead there is a bypass ducting around the exchanger, so as to provide fresh air at outdoor temperature and humidity whenever the outside temperature exceeds 18°C. It is uncommon in Norway to have a humidifier in the air handling unit, but it was added nonetheless to make the energy consumption with and without MEE more comparable. Indeed, the MEE contributes to keeping a satisfactory humidity level, so the energy that would be needed without the MEE to keep the desired level of humidity is taken into account.

The indoor temperature and humidity are assumed to be constant and equal to the set point temperature 21°C and the set point humidity 40%. Thus the set point moisture content is 0.0062 kg/kg. Based on Liu et al. (2017), a simplified frosting limit has been chosen at 0°C [19]. The fan efficiency is assumed to be constant and equal to 12.5%, based on the characteristics of the fans used in the lab, model CK 100A manufactured by Östberg, which are also suitable for this application. The fan efficiency is low due to the low flow rate applied.

Table 5.1: Characteristics of the model

Parameter	Value
Number of MEE channels	36
Flowrate [L/s]	15.6
Fan efficiency [%]	12.5
System pressure drop [Pa]	60
Set point temperature [°C]	21
Set point humidity [%RH]	40
Set point moisture content [kg/kg]	0.0062
Frosting limit [°C]	0

Three different spacers have been modelled: one representing the spacer used in the lab for measurements (“Lab”), a second one with the same corrugation pitch which follows the flow pattern (“Wavy”), and a third one with a straight, larger corrugation (“Large”). The different spacers are represented on figure 5.2.

The hydraulic diameter is calculated according to the shape of the corrugation. It is defined as:

$$D_h = \frac{4A}{P} \quad (5.1)$$

Where A is the cross-sectional area of a channel and P is the perimeter. For a sine shape, a correlation based on aspect ratio can be used [29]. For a trapeze shape, D_h can be directly calculated.

$$D_{h,sine} = 2p\alpha(1.0542 - 0.467\alpha - 0.1180\alpha^2 + 0.1794\alpha^3 - 0.0436\alpha^4) \quad (5.2)$$

$$D_{h,trapeze} = \frac{2b(p - \frac{b}{\tan(\beta)})}{p + b(\frac{1}{\sin(\beta)} - \frac{1}{\tan(\beta)})} \quad (5.3)$$

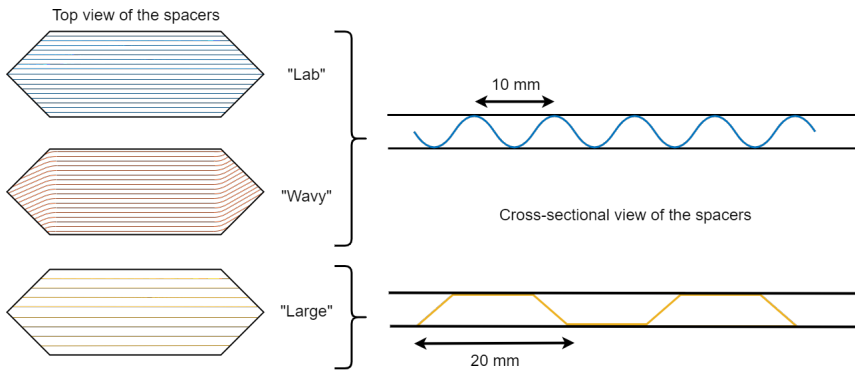


Figure 5.2: Spacers used in the model

Where p is the corrugation pitch; b is the channel height; α is the aspect ratio $\alpha = 2b/2p$; β is the trapeze angle adjacent to the longest side.

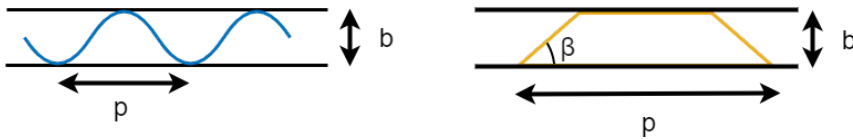


Figure 5.3: Dimensions for hydraulic diameter calculation.

Table 5.2: Properties of the spacers

Spacer	Corrugation pitch	Corrugation shape	Hydraulic diameter
“Lab”	10mm	Sine	3.8 mm
“Wavy”	10mm	Sine	3.8 mm
“Large”	20mm	Trapeze	3.5 mm

5.2 Correlations for Colburn j factor and friction factor f

As the performances of the “Wavy” and “Large” spacers could not be measured in the lab (see page i), hypothetical Colburn j-factors and friction factors were used in the model. The guess was based on correlations established by Woods et al. on the influence of corrugation angle on heat/moisture transfer and pressure drop, and correlations established by Retterstøl, a former master student, on the influence of corrugation size [35, 28].

5.2.1 Influence of spacer angle

To predict the effectiveness and pressure drop with the “Wavy” spacer, the friction factor and Colburn factor have to be guessed for different orientation angles of the spacer with

regards to the flow. Indeed, in the case of the “Lab” spacer, the corrugation will be parallel to the direction of the flow in the counter-part, but not in the cross-part. Thus, the Colburn factor and friction factor are expected to be higher in the cross-parts. The “Wavy” spacer is the same as the “Lab” spacer except that the corrugation is assumed to be parallel to the flow also in the cross-parts.

Two different Colburn factors can directly be obtained by reversing Kays’ solution for quasi-counter flow exchanger effectiveness (table 3.1): given the sensible effectiveness ϵ_t and the areas of the counter- and cross-parts, a NTU for the counter-part and a NTU for the cross part can be obtained from the e2NTU function (Appendix D). From there the Colburn factor can be calculated as in p.30.

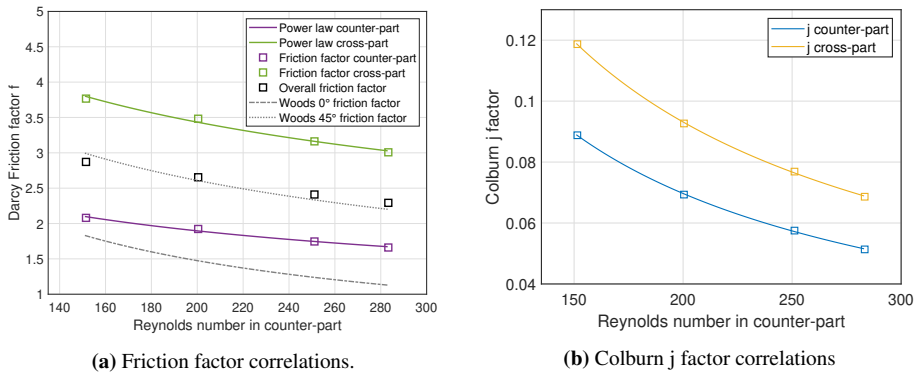


Figure 5.4: Correlations from Woods

On the other hand, only one overall friction factor can be obtained from the pressure drop measured with the “Lab” spacer. Thus, some hypothesis have to be made so as to get two different friction factors, in the cross-parts (f_x) and in the counter-part (f_c). The first hypothesis is that the friction factors in both parts are proportional:

$$f_x = r.f_c \quad (5.4)$$

The direction of the flow is assumed to be angled 45° to the corrugation of the spacer in the cross-parts and 0° in the counter-part. The second hypothesis is that the ratio r is the same as in the study from Woods et al., where the Colburn factor and friction factor of a channel with spacer are investigated for a spacer angled 0°, 45°, and 90° to the direction of the flow. As the ratio r varies with Re , an average value was taken. Then, f_x and f_c can be calculated from the measured pressure drop, as:

$$\Delta P = f_c \frac{2\rho L_c u_c^2}{D_h} + r f_c \frac{2\rho L_c u_c^2}{D_h} \quad (5.5)$$

Thus

$$f_c = \frac{D_h \Delta P}{2\rho(L_c u_c^2 + r L_x u_x^2)} \quad (5.6)$$

$$f_x = r.f_c \quad (5.7)$$

This way, the two friction factors f_x and f_c predict correctly the pressure drop for the lab MEE, just like the overall friction factor f . The correlations obtained are presented in equation 5.10 and figure 5.4a. The code that was used to calculate the correlations is presented in Appendix E.

$$f_x = 23.402.Re^{-0.36} \quad j_x = 9.3095.Re^{-0.87} \quad (5.8)$$

$$f_c = 12.922.Re^{-0.36} \quad j_c = 6.9651.Re^{-0.87} \quad (5.9)$$

$$f = 17.839.Re^{-0.36} \quad (5.10)$$

5.2.2 Influence of corrugation pitch

To guess the friction factor for a spacer with large corrugation, the master thesis results from Retterstøl, a former master student, were used [28]. The ratio between the friction factor they found for a 20mm corrugation pitch and for a 10mm corrugation pitch was applied to the friction factor in equation 5.10 (see fig. 5.5). The resulting friction factor correlation for the “Large” spacer is:

$$f_{large} = \frac{17.839}{1.562}.Re^{-0.36} \quad (5.11)$$

No study was found on Colburn factor correlations for different spacer corrugation pitches. It can be expected that with a larger corrugation, the Colburn factor will be lower. Thus, an arbitrary ratio of 1.2 was chosen as a first guess:

$$j_{x,large} = \frac{9.3095}{1.2}.Re^{-0.87} \quad (5.12)$$

$$j_{c,large} = \frac{6.9651}{1.2}.Re^{-0.87} \quad (5.13)$$

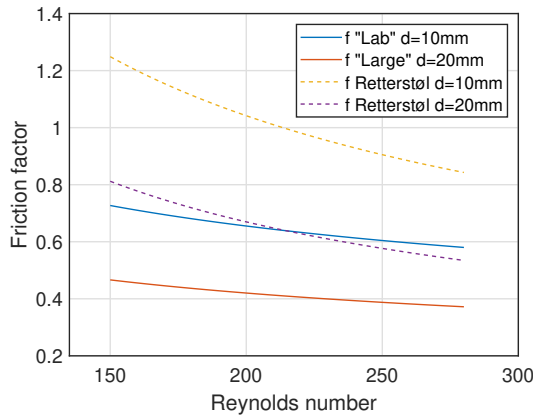


Figure 5.5: Friction factor correlations from Retterstøl [28].
d=corrugation pitch p.

5.3 Verification of model against experimental data

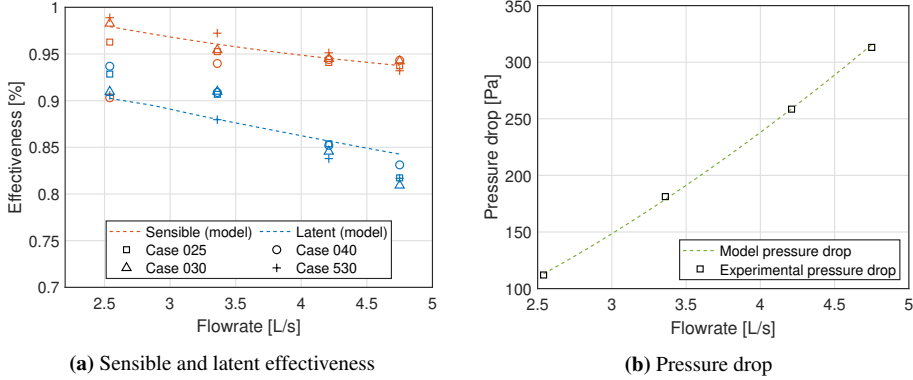


Figure 5.6: Comparison of model results and experimental results

Compared to experimental data, the model of MEE with “Lab” spacer gives acceptable results. If Case 025 is ignored, since it is suspected to have methodical errors in the experimental phase, the model deviation from experimental results is within 1.7% for sensible effectiveness, 4% for latent effectiveness and 1.3% for pressure drop. The model is the least precise for latent effectiveness, but it is also for latent effectiveness that the uncertainty is the highest (around 8%). Nevertheless, it can be observed that the trend of the model curve does not quite follow the trend of experimental data. Indeed, the model calculates latent effectiveness using the Chilton-Colburn analogy, based on the Colburn factor calculated from sensible effectiveness. A way to make it more precise could be to calculate a different Colburn factor for mass transfer from the experimental latent effectiveness, or to implement a variable membrane moisture diffusion resistance as did Al-Waked et al. [2].

5.4 Energy savings calculations

The energy savings were calculated as the difference in enthalpy of humid air, between a system with MEE and a system without MEE. The code can be found in Appendix G. The enthalpy of humid air for one time step is calculated as:

$$H(T, w) = (\dot{m}c_p T + w\dot{m}\Delta h_{lg} + w\dot{m}c_{p,wv}T)\delta t \quad (5.14)$$

Where H is the enthalpy of humid air [J]; \dot{m} is the mass flow rate of air [kg/s]; c_p is the specific heat capacity of air at constant pressure [J/(kg.K)]; w is the water vapor mass fraction; Δh_{lg} is the specific vaporization enthalpy of water [J/kg]; $c_{p,wv}$ is the specific heat capacity of water vapor [J/(kg.K)]; T is the temperature of the air; δt is the time step [s].

For each city, the weather data file contains hourly measurements of temperature and relative humidity. during a whole year. Thus the time step is 3600 seconds.

As there is no cooling or dehumidifying system, different cases are to be taken into account:

- If the temperature and moisture content at the MEE supply outlet are lower than the set points 21°C and 0.0062 kg/kg, the air is conditioned in the room.
- If the outdoor temperature exceeds 18°C, the exchanger is bypassed, and there is no heating of air.
- If the outdoor moisture content exceeds 0.0062 kg/kg, there is no humidifying.
- If the outdoor temperature is below the frosting limit 0°C, preheating has to be used before the MEE.

The calculation of savings considering all the different cases is summed up in table 5.3.

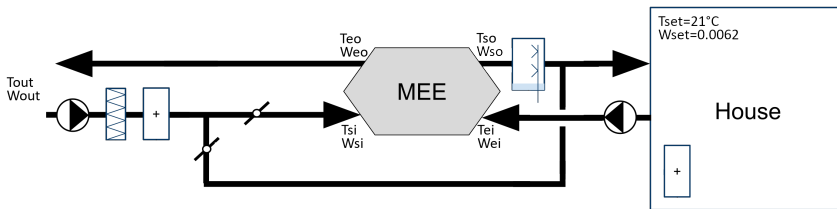


Figure 5.7: Temperature and moisture content labels.

Table 5.3: Energy calculations for all the possible outdoor conditions

	$w_{out} < w_{set}$	$w_{out} > w_{set}$
$T_{out} < 0^{\circ}C$	$Q_{pre} = H(0^{\circ}C, w_{out}) - H(T_{out}, w_{out})$ $Q_{fan} = Q_{fan1}$ $Q_{post} = H(T_{set}, w_{set}) - H(T_{so}, w_{so})$ $Q_0^* = H(T_{set}, w_{set}) - H(T_{out}, w_{out})$	$Q_{pre} = H(0^{\circ}C, w_{out}) - H(T_{out}, w_{out})$ $Q_{fan} = Q_{fan1}$ $Q_{post} = H(T_{set}, w_{so}) - H(T_{so}, w_{so})$ $Q_0^* = H(T_{set}, w_{out}) - H(T_{out}, w_{out})$
$0^{\circ}C < T_{out}$ $T_{out} < 18^{\circ}C$	$Q_{pre} = 0$ $Q_{fan} = Q_{fan1}$ $Q_{post} = H(T_{set}, w_{set}) - H(T_{so}, w_{so})$ $Q_0^* = H(T_{set}, w_{set}) - H(T_{out}, w_{out})$	$Q_{pre} = 0$ $Q_{fan} = Q_{fan1}$ $Q_{post} = H(T_{set}, w_{so}) - H(T_{so}, w_{so})$ $Q_0^* = H(T_{set}, w_{out}) - H(T_{out}, w_{out})$
$T_{out} > 18^{\circ}C$	$Q_{pre} = 0$ $Q_{fan} = Q_{fan0}$ $Q_{post} = 0$ $Q_0^* = 0$	$Q_{pre} = 0$ $Q_{fan} = Q_{fan0}$ $Q_{post} = 0$ $Q_0^* = 0$

Then the energy consumed with MEE Q_{tot} and the energy consumed without MEE

Q_0 are calculated as:

$$Q_{tot} = Q_{pre} + Q_{fan} + Q_{post} \quad (5.15)$$

$$Q_0 = Q_0^* + Q_{fan0} \quad (5.16)$$

Where Q_{pre} is the energy consumed for preheating; Q_{fan} is the energy consumed by the fan; Q_{post} is the energy consumed for conditioning after the MEE; Q_0^* is the energy consumed for conditioning of air without MEE; Q_{fan0} is the energy consumed by the fan without MEE, or when using the bypass, during one time step. Q_{fan1} (in table 5.3) is the energy consumed by the fan with MEE during one time step. Finally, the energy savings are:

$$Savings = Q_0 - Q_{tot} \quad (5.17)$$

The calculation is iterated for all the hours of the year. The result is a *Savings* vector containing hourly savings. The yearly saved energy is the sum of all the *Savings* vector elements.

Results and discussion

6.1 Experiments results

Figure 6.1 shows the experimental effectiveness as a function of exhaust inlet relative humidity RH_{ei} and supply inlet temperature T_{si} . From fig.6.1a, it seems that latent effectiveness decreases with RH_{ei} , while sensible effectiveness increases with RH_{ei} . A linear regression has been performed for each flowrate, without time-averaging the time series, removing the suspicious Case 025 at 2.5 L/s (Appendix M). Indeed, linear regressions show a strong positive correlation between sensible effectiveness and exhaust relative humidity ($R^2 = 0.5 - 0.8$); and a weak negative correlation between latent effectiveness and supply relative humidity ($R^2 = 0.05 - 0.3$). Albdoor et al. (2019), also found that moisture diffusivity and latent effectiveness decreased with increasing moisture difference, but they had a strong correlation. It seems that linear coefficient decreases with increasing flowrate, that is to say exhaust relative humidity has more influence on effectiveness at low flowrates.

Concerning supply inlet temperature, all the cases had 0°C in the cold room, except for Case 530 which had 5°C . It is therefore difficult to conclude anything on the correlation or lack thereof between supply inlet temperature and effectiveness. It can however be noted that supply inlet temperature and air flow rates are not independent variables: the highest the flowrate, the lowest the supply inlet temperature. That can be explained by the transportation of air from the cold room to the MEE through insulated ducts in a $19\text{-}20^\circ\text{C}$ environment. A higher flow rate means a shorter travel time from the cold room to the MEE and thus less heat transfer from the ambient air to the cold supply air.

It can be observed on figure 6.1b that for each flow rate the measurements of effectiveness and supply inlet temperature are close together for the three cases with 0°C in the cold room, and Case 530 can be identified for each flow rate by having a similar effectiveness but higher T_{si} . There is an outlier point at 2.5 L/s, which corresponds to Case 025, the case which is suspected to contain experimental errors. The figure shows that the supply inlet temperature for this point is lower than expected. We can thus hypothesize that the error may be a wrong setting of the flowrate.

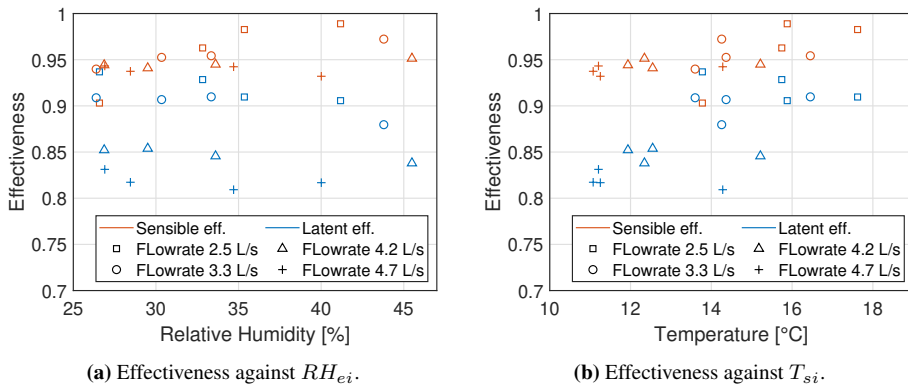


Figure 6.1: Experimental effectiveness results against indoor relative humidity and supply inlet temperature conditions.

6.2 Model results

Using the MATLAB model described in chapter 5, the energy savings have been calculated for the small house using a MEE with three different spacers, in three Norwegian cities, Trondheim, Oslo and Bergen (fig. 6.2a). The energy savings are highest for Trondheim, followed by Oslo and Bergen, which is in the order of decreasing heating demand. Indeed, Trondheim has the highest sensible heating demand with 5490 degree.days, Oslo has 5250 degree.days and Bergen 5080 degree.days. Bergen also has the lowest humidifying demand as it is a very humid city. The latent energy consumed in Bergen is approximately 25% lower than in Trondheim or Oslo. Since the energy needs are lower in Bergen, the energy savings are lower too.

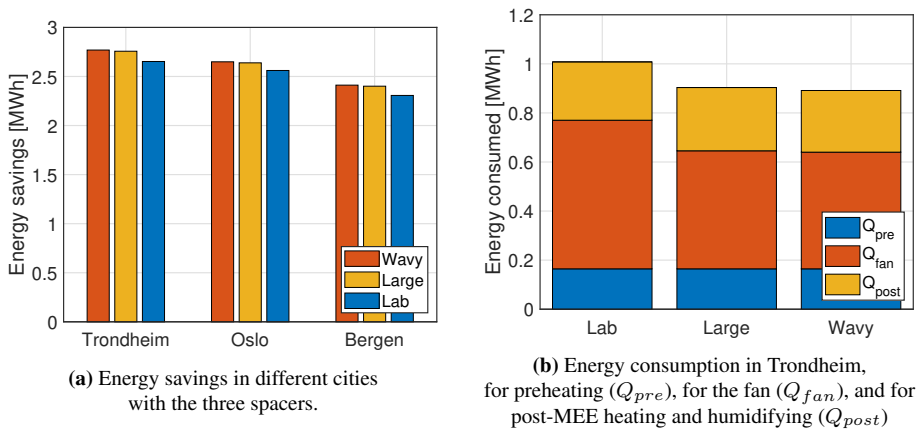


Figure 6.2: Energy savings and energy consumption results from the model.

In all the three cities, the savings are higher with the “Wavy” spacer, followed closely by the “Large” spacer, and the “Lab” spacer which gives lower savings. The savings with “Wavy” and “Large” spacer are 3.0-4.6% larger than the savings with “Lab” spacer. It can be guessed that a spacer which has both a large corrugation pitch and the wavy pattern could give significantly higher savings given the fact that there are no additional costs of fabrication, hence the importance of carefully designing spacers for low pressure drop.

Looking closer at the different loads for the three spacers in Trondheim (fig. 6.2b), we can observe the trade-off between pressure drop and effectiveness, as the energy consumption for post-conditioning is lower with “Lab” spacer, but energy consumption for the fan is higher. In the case of the “Lab” spacer, the fan represents 57% of the total energy consumed and space heating represents 24%. For the “Wavy” and “Large” spacers, the energy for the fan and space heating represent respectively 50% and 28%. Since most of the energy is consumed by the fan (Q_{fan} on figure 6.2b), the savings are lower with the “Lab” spacer, despite the fact that less post-conditioning is needed (Q_{post} on figure 6.2b). In this case, the fan efficiency is low (12.5%) and the energy demand for the fan is the highest. Usually fan efficiencies range between 25-50%. If this was a real system, the priority to increase energy savings would be to improve the fan efficiency, then, to reduce pressure drop.

Nasif et al. found that the savings from a MEE compared to a conventional air mixing system are highest for hot and humid climate and lowest for cold climate, because the difference between the MEE and the conventional system appears best when the MEE is used as a dehumidifier as well as heat exchanger. Here, we calculated absolute savings (i.e. compared to the absence of heat recovery) to compare them with each other, and we found that the highest savings are in cities with both a high sensible demand and a high latent demand. Both cases show that the latent energy demand has significant impact on the energy savings potential of an MEE.

Unlike Koester et al., we found that the spacers which enhance enthalpy transfer the most were increasing fan energy consumption more than it was reducing space heating and humidifying. However, the trade-off balance could be different with a higher fan efficiency. Different possibilities with geometry and fan efficiencies will be explored in the next section.

6.2.1 Parametric analysis

The influence of several parameters on effectiveness, pressure drop, and energy savings has been investigated for the “Lab” spacer. The shape of the MEE, the channel spacing and the hydraulic diameter have been studied, for different fan efficiencies. The energy savings were calculated for fan efficiencies of 12.5%, 25% and 50% to capture a range of possible behaviours when changing a geometrical parameter. As previously, the energy savings were calculated over the whole year in the small house described in chapter 5, and the house was located in Trondheim.

Shape of the MEE

MEEs in quasi-counterflow configuration can come in various shapes, depending on the length and width of the counter-part. The effectiveness and pressure drop of the MEE have been calculated for different widths and lengths. To make the results comparable, the transfer area was kept constant. This was done by using the width-to-length ratio a/L as the parameter of interest instead of the width and length separately. Then, knowing the area of one membrane layer A_{tot} , calculating the corresponding length L and width a :

$$r_{aL} = \frac{a}{L} \quad (6.1)$$

$$A_{tot} = 0.13125 \text{ m}^2 \quad (6.2)$$

$$a = \sqrt{\frac{A_{tot}}{\frac{1}{r_{aL}} + \frac{1}{2}}} \quad (6.3)$$

$$L = \frac{a}{r_{aL}} \quad (6.4)$$

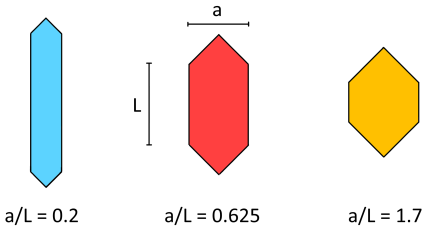


Figure 6.3: Shape of the MEE with different a/L ratios.

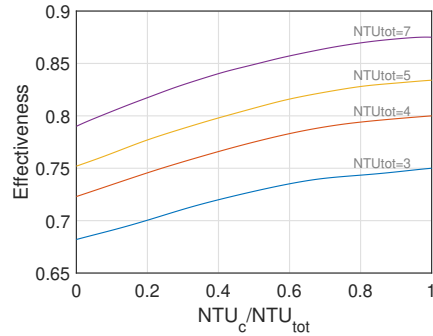


Figure 6.4: Effectiveness with increasing share of NTU in the counter-part. From Kays et al. [13].

A second condition to the calculation of a and L was that the cross-like headers are square-angled, as it is a condition to be able to use the ϵ -NTU solution from Kays et al. (table 3.1).

The performances for different a/L ratios are presented in fig. 6.5a. It can be seen that the closer the shape is to a cross-flow configuration (high a/L ratio), the lower are the sensible and latent effectiveness. Indeed, the NTU is proportional to the Nusselt number and to the transfer surface area. When the a/L ratio increases with constant total transfer area, the cross-part area increases and the counter-part area decreases. Thus NTU_x increases with a/L and NTU_c decreases with increasing a/L , which decreases the effectiveness as can be seen on figure 6.4.

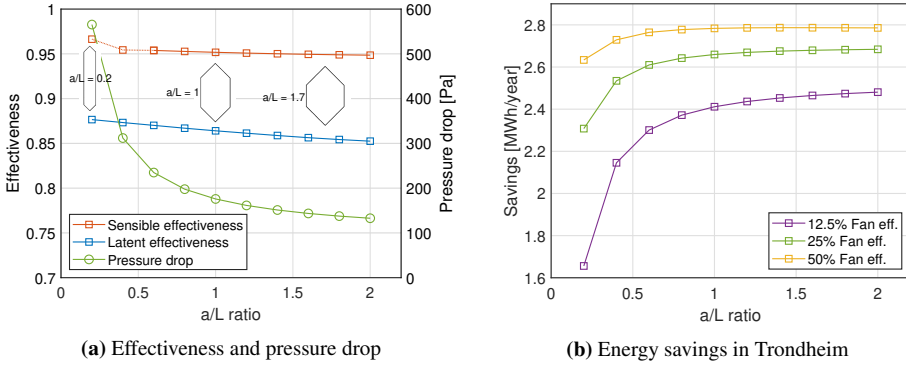


Figure 6.5: Performances of the MEE with varying a/L ratio and constant transfer area.

In theory, the Nusselt number Nu should be independent from Re . Then, the only effect on effectiveness would be the distribution of transfer area between cross- and counter-part. However, experimentally Nu depends on Re to some extent, as the experimental Colburn factor correlations are based on the following power law:

$$j = C_1 Re^{-m} \quad C_0 > 0 \text{ and } 0 < m < 1 \quad (6.5)$$

And

$$Nu = j Re Pr^{1/3} \quad (6.6)$$

$$Nu = C_1 Re^{1-m} Pr^{1/3} \quad (6.7)$$

In this model and as in studies from Liu et al. and Woods et al. [22, 35], Nu is a decreasing function of Re . When a/L increases, the air channels become larger and the air velocity and Reynolds number become smaller. Therefore there are competing effects, as the decreasing Re tends to increase effectiveness, and at the same time the distribution of cross- and counter- transfer surface area tends to decrease effectiveness. Here, the distribution of transfer area is the predominant effect. The effectiveness results marked with a dotted line may be unrealistic due to oscillations in the extrapolation method (see p.51).

While the sensible and latent effectiveness seem to decrease linearly with decreasing a/L ratio, it is not the case for pressure drop. Indeed, the major contributions to pressure drop are the friction losses in the cross-parts, which are proportional to the length of the cross-parts c ; and the friction loss in the counter-parts, which is proportional to the length of the counter-part L . As c is proportional to r_{aL} , and L is proportional to $1/r_{aL}$, it follows that the pressure drop shoots up to very high values when a/L is close to 0. From there it can be predicted that the pressure drop will be the main factor limiting energy savings, especially for low a/L ratio and low effectiveness.

The energy savings for different fan efficiencies can be seen in fig.6.5b. For low fan efficiencies, it can be seen, that the pressure drop is by far the dominant factor in limiting energy savings, and energy savings only increase with a/L ratio. For high efficiencies, the effectiveness appears as a limiting factor for higher a/L ratios. At 50% fan efficiency the trade-off between effectiveness and pressure drop is visible: energy savings reach a

maximum around $a/L = 1.5$, which shows the switch from pressure drop to effectiveness as limiting factors. Additionally to fan efficiency, outdoor temperature also influences to what extent lower pressure drop should be preferred over higher effectiveness. In cold regions where the heating load is high, it is more important to have high sensible effectiveness than in milder regions, where the heating load will not be as high compared to the fan load.

Channel spacing

The effectiveness, pressure drop, and energy savings results for different channel spacings are shown on fig.6.6. The volume flow rate and the number of channels are kept constant, which means that as the channel spacing increases the velocity decreases.

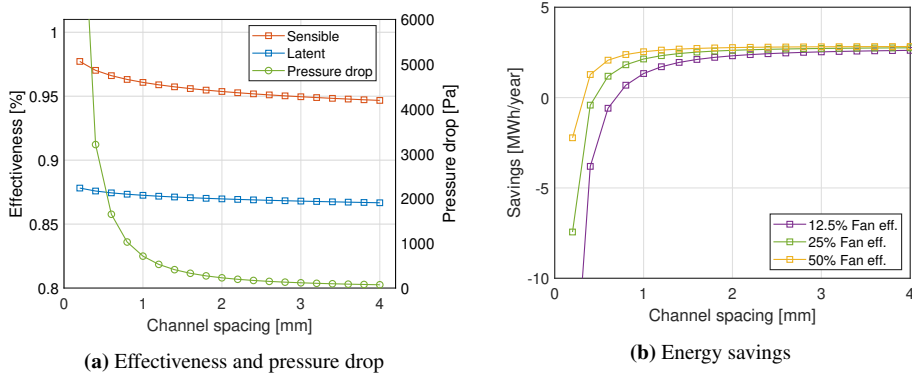


Figure 6.6: Performances of the MEE with varying channel spacing b and constant flow rate.

Higher channels means a reduced Re but also a larger hydraulic diameter, which are competing effects to respectively increase and reduce the NTU. It seems that the influence of channel spacing on effectiveness is quite small, as there is 3% maximum variation for sensible effectiveness and 1% for latent effectiveness. However, in this case the model is inaccurate since it uses experimental Colburn factor correlations that were measured for constant channel spacing. It means that although Nu is supposed to depend on the geometry of the channel, in this model Nu is constant for all the channel spacings. This is especially relevant to notice for channel spacing, because changing the channel spacing will change the aspect ratio, whereas changing the a/L ratio or the hydraulic diameter does not necessarily change the aspect ratio.

The pressure drop is proportional to $1/b$, where b is the channel spacing, and to u^2 where u is the velocity of air. When the channel spacing increases and the velocity decreases, both of these effects contribute to reducing the pressure drop, although the friction factors are slightly higher for a smaller Re . The resulting pressure drop can be seen on fig.6.6a.

The energy savings are shown fig.6.6b. For all fan efficiencies, the savings become negative for channel spacings under 1mm, which means that more energy is spent on pushing the air through the system than the energy recovered. For channels higher than 2

mm, the savings seem to become constant. If the model featured a Nusselt number that changes according to channel geometry, it can be guessed that the energy savings would reach a maximum and then decrease for larger channel spacings.

Hydraulic diameter

The hydraulic diameter is representative of how the shape of the channel, or the spacers, affects the flow. Confirming the findings from Al-Waked et al. [2], the hydraulic diameter seems to have a large influence on the sensible and latent effectiveness [2]. The influence of hydraulic diameter is more important than that of the shape of the exchanger for example. For the same flow rate and cross-sectional area, a channel with smaller D_h will have better heat and moisture transfer due to more surface of contact between the fluid and the wall of the channel, but also higher pressure drop. Conversely, a channel with bigger hydraulic diameter will have less heat and moisture transfer and also less pressure drop.

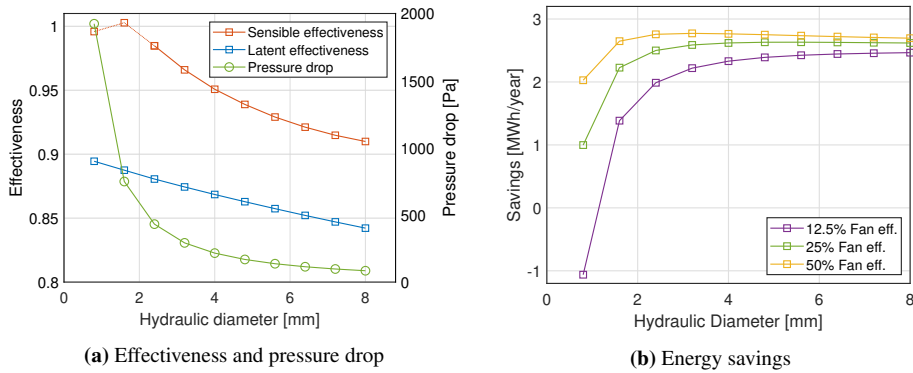


Figure 6.7: Performances of the MEE with varying hydraulic diameter.

Figure 6.7b shows that the higher is the fan efficiency the smaller is the optimal hydraulic diameter. For low fan efficiencies and small D_h , the pressure drop is the factor limiting energy savings, whereas for high fan efficiencies and high D_h , the effectiveness is the factor limiting the energy savings. A hydraulic diameter of 4mm corresponds to a 2mm rectangular empty channel. Thus, while keeping the same channel height, with different shapes of spacers the hydraulic diameter can be changed within 0 and 4mm. For example, figure 6.8 shows the variation of hydraulic diameter with the shape a trapeze channel of constant height and width. Then, to obtain a hydraulic diameter between 4 and 8mm, a larger channel spacing would be required.

There is a noticeable anomaly in the sensible effectiveness for smaller hydraulic diameters. This is due to the fact that the ϵ -NTU solution from table 3.1 is only given for NTU_x and NTU_c under 7. As in this case, the NTUs are larger than 7, the 2D table was extrapolated using akima polynomials. Although the interpolation method gives less oscillations than the spline method, for very large NTUs some oscillations still show. The effectiveness results that are not reliable due to oscillations are shown on figure 6.5a and on figure 6.7a with a dotted line. We can see on figure 6.9 that oscillations appear for high values of NTU_c and low values of NTU_x .

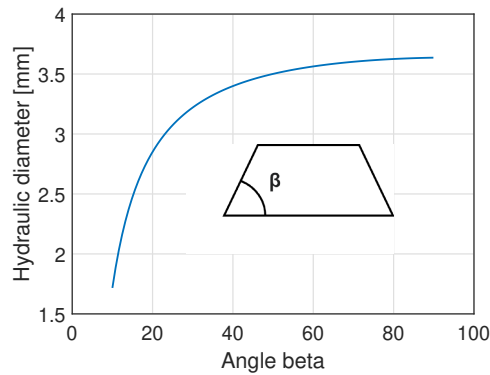


Figure 6.8: Hydraulic diameter of trapezoidal channel with varying beta angle, constant height=2mm and constant width=20mm (long side).

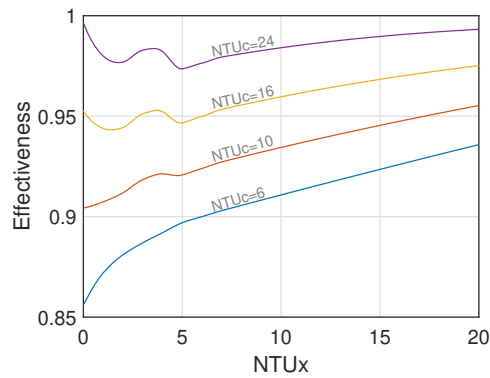


Figure 6.9: Effectiveness from the KaysEff function (Appendix C).

6.3 Advantages and limitations of the model

One of the main advantages of using a ϵ -NTU model compared to CFD is its simplicity. Although it is a very simple model, it could predict the sensible effectiveness and pressure drop with a deviation under 2% and latent effectiveness with a deviation within 4%. The simplicity and short computation time allows quite easily to loop through the model to test different values for chosen parameters, as was done in section 6.2.1.

A disadvantage of the ϵ -NTU model is that for quasi-counterflow configuration, there is no analytical correlation between the NTU and the effectiveness. The numerical solution from Kays can be interpolated to find the desired values, but most of our values lie outside the domain of the solution. As the results of the extrapolation can vary depending on the method used and the chosen boundary conditions, there is a certain range of effectiveness within which the result solely depends on the operator’s modelling choices.

Yet, the most important limitation lies in the lack of experimental and analytical data concerning the influence of spacer angle and spacer corrugation pitch on the performances.

Based on the available studies, an attempt to make a realistic guess was formulated, but an experimental investigation would be needed to confirm or refute the potential of the proposed spacers.

Another important factor when studying wire mesh spacers is the wire diameter and mesh size, which have impacts on the pressure drop and effectiveness. Those two factors are not taken into account by the model. Additionally, when the effectiveness was calculated for different channel spacings and hydraulic diameters, the Nusselt number was kept constant. Indeed, it is difficult to calculate a theoretical Nusselt number which corresponds to the actual flow conditions because the flow is disrupted by the presence of the spacer, which means that the conditions for validity of the theoretical correlations are not fulfilled. However, the Nusselt number is dependent on the geometry of the channels and in a real situation the Nusselt number would vary with the shape of the channel.

Lastly, since the energy savings are calculated with regards to the set point indoor temperature and relative humidity only, it is equivalent to modelling a house with constant indoor temperature and relative humidity. The frosting limit of the exchanger is dependent on indoor relative humidity and outdoor temperature. With constant indoor relative humidity, the model can have a simplified temperature-only frosting limit. The temperature-only frosting limit has the advantage of being easy to implement, but the disadvantage of concealing the potential additional savings on preheating due to lower frosting limit for a MEE compared to a heat exchanger.

Conclusions and further work

Characteristics of a membrane energy exchanger (MEE) have been measured experimentally to provide the basis for a performance prediction model. Performances have been measured under different conditions of supply temperature and exhaust humidity. A strong positive correlation was found between sensible effectiveness and exhaust relative humidity, and a weak negative correlation between latent effectiveness and exhaust relative humidity. No conclusions could be drawn on the influence of supply temperature on effectiveness. From effectiveness and pressure drop measurements, correlations have been established for the Colburn factor and friction factor in the lab MEE. These correlations have been used to create a MATLAB model which predicts the effectiveness and pressure drop of the lab MEE with a deviation under 1.7% for sensible effectiveness, 4% for latent effectiveness and 1.3% for pressure drop. Then the correlations coupled with other studies were used to make an informed guess of the performances of the MEE with different spacers. The model was extended to calculate the yearly energy savings for a small house in Trondheim, Bergen and Oslo.

It was found that the spacer which is shaped like the flow patterns and the spacer with a larger corrugation pitch can potentially provide higher energy savings than the spacer used in the lab, because they can provide a lower pressure drop. The model has been used to carry out a parametric analysis in order to see how the shape of the MEE, the channel spacing and the hydraulic diameter influence the effectiveness, pressure drop and energy savings. It was found that pressure drop is often the limiting factor for energy savings, especially for low fan efficiencies. At higher fan efficiencies, the effectiveness can sometimes become the limiting factor for energy savings. Concerning the shape of the MEE, higher energy savings are found for short and wide exchangers which favor low pressure drop, although for higher fan efficiencies, savings may decrease when the shape becomes closer to a cross-flow than to a quasi-counter flow. It is important for channel spacing not to be too small otherwise the pressure drop becomes so high that no energy savings can be achieved. However, higher channels are expected to reduce heat and mass transfer, which did not appear in the simulation because the Nusselt and Sherwood number were

measured for constant channel spacing. Finally, hydraulic diameter was found to have the most impact on effectiveness, which translates into a more visible trade-off: with low fan efficiency, when mostly pressure drop is limiting energy savings, the optimal hydraulic diameter is larger than with high fan efficiency, when mostly effectiveness is limiting energy savings.

A spacer has been fabricated in the lab which has both a shape close to the flow pattern and a large corrugation pitch. The fabrication process has been detailed for further use. Further work on this subject could include:

- Experimental investigation of the proposed spacers, to measure and compare their energy savings potentials.
- Experimental validation of an optimized shape based on the theoretical study.
- Modelling of a more accurate frosting limit. Frosting limits depend on outdoor temperature, indoor humidity and effectiveness. Higher energy savings can be obtained if the threshold at which preheating is needed is lowered. These savings can be modelled if the frosting limit is calculated based on the aforementioned parameters.
- Improve the model for latent effectiveness. Variable membrane moisture resistance can be explored.

Bibliography

- [1] 2005 ASHRAE Handbook: Fundamentals, ASHRAE, 2005.
- [2] R. Al-Waked et al., CFD simulation of air to air enthalpy heat exchanger: Variable membrane moisture resistance, *Applied Thermal Engineering*. 84:301–309, 2015.
- [3] R. Al-Waked, M. S. Nasif, and D. B. Mostafa, Enhancing the performance of energy recovery ventilators, *Energy Conversion and Management*. 171:196–210, 2018.
- [4] A. K. Albdoor, Z. Ma, and P. Cooper, Experimental investigation and performance evaluation of a mixed-flow air to air membrane enthalpy exchanger with different configurations, *Applied Thermal Engineering*. 166:114–682, 2020.
- [5] A. K. Albdoor, Z. Ma, and P. Cooper, Moisture diffusion measurement and evaluation for porous membranes used in enthalpy exchangers, *Energy Procedia*. 160:499–506, 2019.
- [6] ANSI/ASHRAE Standard 62.1-2019, Ventilation for Acceptable Indoor Air Quality, technical report, 2019.
- [7] G. Baldinelli et al., Experimental analysis of an innovative organic membrane for air to air enthalpy exchangers, *International Communications in Heat and Mass Transfer*. 108:104–332, 2019.
- [8] C. Beattie et al., Experimental study of air-to-air heat exchangers for use in arctic housing, *Applied Thermal Engineering*. 129:1281–1291, 2018.
- [9] T. L. Bergman et al., Fundamentals of Heat and Mass Transfer, John Wiley & Sons, 2011.
- [10] Y.-h. Choi et al., Analysis of the variable heat exchange efficiency of heat recovery ventilators and the associated heating energy demand, *Energy and Buildings*. 172:152–158, 2018.
- [11] M. Evensen, An Experimental Investigation of a Quasi-Counter-Flow Air-to-Air Membrane Energy Exchanger, PhD thesis, Trondheim, Norway: Norwegian University of Science and Technology, 2019.
- [12] M. Fehrm, W. Reiners, and M. Ungemach, Exhaust air heat recovery in buildings, *International Journal of Refrigeration*. 25 (4):439–449, 2002.

-
- [13] W. M. Kays, R. K. Jain, and S. Sabherwal, The effectiveness of a counter-flow heat exchanger with cross-flow headers, *International Journal of Heat and Mass Transfer*. 11 (4):772–774, 1968.
- [14] W. M. Kays and A. L. London, *Compact Heat Exchangers*, Krieger Publishing Company, 1984.
- [15] N. Kho et al., Performance characterization of the membrane-based energy recovery system, *Procedia Engineering*. 214:50–58, 2017.
- [16] S. Koester et al., Spacer enhanced heat and mass transfer in membrane-based enthalpy exchangers, *Journal of Membrane Science*. 520:566–573, 2016.
- [17] S. Lecomte-Saur, Measurement and analysis of membrane heat exchanger for energy efficient ventilation, Project work, Trondheim, Norway: Norwegian University of Science and Technology, 2019.
- [18] P. Liu, Energy Recovery with Air-to-air Membrane Energy Exchanger for Ventilation in Cold Climate, PhD thesis, Trondheim, Norway: Norwegian University of Science and Technology, 2016.
- [19] P. Liu et al., A frosting limit model of air-to-air quasi-counter-flow membrane energy exchanger for use in cold climates, *Applied Thermal Engineering*. 111:776–785, 2017.
- [20] P. Liu et al., A theoretical model to predict frosting limits in cross-flow air-to-air flat plate heat/energy exchangers, *Energy and Buildings*. 110:404–414, 2016.
- [21] P. Liu et al., Energy transfer and energy saving potentials of air-to-air membrane energy exchanger for ventilation in cold climates, *Energy and Buildings*. 135:95–108, 2017.
- [22] P. Liu et al., Performance of a quasi-counter-flow air-to-air membrane energy exchanger in cold climates, *Energy and Buildings*. 119:129–142, 2016.
- [23] J. Mulder, *Basic Principles of Membrane Technology*, Springer Science & Business Media, 2012.
- [24] M. S. Nasif and R. Al-Waked, Seasonal Weather Conditions Effect on Energy Consumption and CO₂ Emission for Air Conditioning Systems Coupled with Enthalpy Energy Recovery Heat Exchanger, *APCBEE Procedia*. 10:42–48, 2014.
- [25] B. K. Paul, S. Kawula, and C. Song, A manufacturing process design for producing a membrane-based energy recovery ventilator with high aspect ratio support ribs, *Journal of Manufacturing Systems*. 52:242–252, 2019.
- [26] S. Qiu et al., An energy exchange efficiency prediction approach based on multivariate polynomial regression for membrane-based air-to-air energy recovery ventilator core, *Building and Environment*. 149:490–500, 2019.
- [27] M. Rafati Nasr et al., A review of frosting in air-to-air energy exchangers, *Renewable and Sustainable Energy Reviews*. 30:538–554, 2014.
- [28] A. Retterstøl, Design of membrane energy exchanger concerning pressure loss, PhD thesis, Norwegian University of Science and Technology, 2018.

-
- [29] R. K. Shah and D. P. Sekulic, *Fundamentals of Heat Exchanger Design*, John Wiley & Sons, 2003.
- [30] D. Siegele and F. Ochs, Effectiveness of a membrane enthalpy heat exchanger, *Applied Thermal Engineering*. 160:114–005, 2019.
- [31] SINTEF and Norges teknisk-naturvitenskapelige universitet, ENØK i bygninger: effektiv energibruk, 3. utg., Oslo: Gyldendal undervisning, 2007.
- [32] Siri, Direktoratet for byggkvalitet, URL: <https://dibk.no/byggereglene/byggteknisk-forskrift-tek17/>.
- [33] Summary for Policymakers — Global Warming of 1.5 °C, URL: <https://www.ipcc.ch/sr15/chapter/spm/>.
- [34] I. E. A. a. the United Nations Environment Programme, 2019 Global Status Report: Towards a zero-emission, efficient and resilient buildings and construction sector, 2019.
- [35] J. Woods and E. Kozubal, Heat transfer and pressure drop in spacer-filled channels for membrane energy recovery ventilators, *Applied Thermal Engineering*. 50 (1):868–876, 2013.
- [36] J. Xu et al., Performance study of sodium alginate-nonwoven fabric composite membranes for dehumidification, *Applied Thermal Engineering*. 128:214–224, 2018.
- [37] L.-Z. Zhang, Progress on heat and moisture recovery with membranes: From fundamentals to engineering applications, *Energy Conversion and Management*. 63:173–195, 2012.
- [38] L.-Z. Zhang and E. B. Zelik, *Total Heat Recovery: Heat and Moisture Recovery from Ventilation Air*, New York, UNITED STATES: Nova Science Publishers, Incorporated, 2008.
- [39] Q. Zhong et al., An optimized crossflow plate-fin membrane-based total heat exchanger, *Energy and Buildings*. 86:550–556, 2015.

Appendix A: Risk assessment

NTNU	Hazardous activity identification process			Prepared by HSE section	Number HMSRV2601E	Date 09.01.2013
HSE				Approved by The Rector		Replaces 01.12.2006

Unit: *EPT* Date: **30/06/2020**

Line manager:

Participants in the identification process (including their function):

Short description of the main activity/main process: Master project for student Seylamouni Lecomte-Saur: Measurement and analysis of membrane energy exchanger.

Is the project work purely theoretical? (YES/NO): NO

Answer "YES" implies that supervisor is assured that no activities requiring risk assessment are involved in the work. If YES, briefly describe the activities below. The risk assessment form need not be filled out.

Signatures: Responsible supervisor: *Dr. J. A. J. J.*

Student: *[Signature]*

ID nr.	Activity/process	Responsible person	Existing documentation	Existing safety measures	Laws, regulations etc.	Comment
	Running experiments at the membrane energy exchanger test rig	Seylamouni Lecomte-Saur	NO	NO	NO	

NTNU	Risk assessment			Prepared by	Number	Date
				HSE section	HMSRV2603E	04.02.2011
HSE/KS				Approved by		Replaces
				The Rector		01.12.2006




Unit: EPT

Date: 30/06/2020

Line manager:

Participants in the identification process (including their function):

Short description of the main activity/main process: Master project for student Seylamouni Lecomte-Saur: Measurement and analysis of membrane energy exchanger.

Signatures: *Responsible supervisor:* 

Student: 

Activity from the identification process form	Potential undesirable incident/strain	Likelihood (1-5)	Consequence:		Risk Value (human)	Comments/status Suggested measures
			Human (A-E)	Environment (A-E)		
Running experiments at the membrane energy exchanger test rig	Irritating fiberglass insulation debris spread when opening ducts/checking for leakages.	4	A	A	A4	Wear gloves and long sleeves, clean surfaces after manipulating the insulation material.

Likelihood, e.g.:

1. Minimal
2. Low
3. Medium
4. High
5. Very high

Consequence, e.g.:

- A. Safe
- B. Relatively safe
- C. Dangerous
- D. Critical
- E. Very critical

Risk value (each one to be estimated separately):

- Human = Likelihood x Human Consequence
- Environmental = Likelihood x Environmental consequence
- Financial/material = Likelihood x Consequence for Economy/material

Potential undesirable incident/strain

Identify possible incidents and conditions that may lead to situations that pose a hazard to people, the environment and any materiel/equipment involved.

NTNU		Risk assessment		Prepared by	Number	Date
	HSE/KS			HSE section	HMSRV2603E	04.02.2011
				Approved by		Replaces
		The Rector		01.12.2006		



Criteria for the assessment of likelihood and consequence in relation to fieldwork

Each activity is assessed according to a worst-case scenario. Likelihood and consequence are to be assessed separately for each potential undesirable incident. Before starting on the quantification, the participants should agree what they understand by the assessment criteria:

Likelihood	Low 2	Medium 3	High 4	Very high 5
Minimal 1	Once every 10 years or less	Once a year or less	Once a month or less	Once a week

Consequence

Grading	Human	Environment	Financial/material
E Very critical	May produce fatality/ies	Very prolonged, non-reversible damage	Shutdown of work >1 year.
D Critical	Permanent injury, may produce serious health damage/sickness	Prolonged damage. Long recovery time.	Shutdown of work 0.5-1 year.
C Dangerous	Serious personal injury	Minor damage. Long recovery time	Shutdown of work < 1 month
B Relatively safe	Injury that requires medical treatment	Minor damage. Short recovery time	Shutdown of work < 1week
A Safe	Injury that requires first aid	Insignificant damage. Short recovery time	Shutdown of work < 1day

The unit makes its own decision as to whether opting to fill in or not consequences for economy/materiel, for example if the unit is going to use particularly valuable equipment. It is up to the individual unit to choose the assessment criteria for this column.

Risk = Likelihood x Consequence

Please calculate the risk value for "Human", "Environment" and, if chosen, "Economy/materiel", separately.

About the column "Comments/status, suggested preventative and corrective measures":

Measures can impact on both likelihood and consequences. Prioritise measures that can prevent the incident from occurring; in other words, likelihood-reducing measures are to be prioritised above greater emergency preparedness, i.e. consequence-reducing measures.

Risk matrix



MATRIX FOR RISK ASSESSMENTS at NTNU

		LIKELIHOOD				
CONSEQUENCE		E1	E2	E3	E4	E5
Extremely serious	D1	D1	D2	D3	D4	D5
Serious	C1	C1	C2	C3	C4	C5
Moderate	B1	B1	B2	B3	B4	B5
Minor	A1	A1	A2	A3	A4	A5
Not significant		Very low	Low	Medium	High	Very high

Principle for acceptance criteria. Explanation of the colours used in the risk matrix.

Colour	Description
Red	Unacceptable risk. Measures must be taken to reduce the risk.
Yellow	Assessment range. Measures must be considered.
Green	Acceptable risk Measures can be considered based on other considerations.

Appendix B: Calculation of membrane diffusivity

The manufacturer of the membrane measured the water vapor transfer and provided a value for the membrane moisture diffusivity. However, the value and the dimension of the given membrane diffusivity did not match the theoretical latent effectiveness calculations and the experimental results. Indeed, for the theoretical latent effectiveness calculation a diffusivity in $m^2/(Pa.s)$ is needed, but the value given by the manufacturer was in m^2/s . Furthermore, using this value led to a theoretical latent effectiveness which was very far from the experimental results. Thus, a different value of the moisture diffusivity has been calculated based on the water vapor transfer.

Table 7.1: Values given by the manufacturer

Parameter	Symbol	Value
Water vapor transfer, at 25°C, with one air stream dry and the other at 50% RH	J_m	$8.4 \text{ kg}/(\text{m}^2.\text{day})$
Membrane moisture diffusivity	D_{p0}	$1.6 \times 10^{-12} \text{ m}^2/\text{s}$
Membrane thickness	δ	0.032 mm

The water vapor volume flux though the membrane is expressed as:

$$J = 1.63 \times 10^5 D_p \frac{\Delta w}{\delta} \quad (7.1)$$

Where $J = J_m/\rho$ in $m^3/(m^2.s)$. The factor $1.63 \times 10^5 Pa$ is the additional partial pressure of water vapor for each additional kg of water vapor per kg of air. It is proportional to the ambient pressure (see 3.3.2). Thus:

$$D_p = \frac{\delta \cdot J_m}{1.63 \times 10^5 \cdot \Delta w \cdot \rho} \quad (7.2)$$

From section 3.3.2 we have:

$$1.63 \times 10^5 \Delta w = \Delta RH \cdot P_{sat} \quad (7.3)$$

And using the following equation to find P_{sat} [22]:

$$P_{sat} = 1.629 \times 10^{11} \exp(-5294/T) \quad (7.4)$$

With $T = 298K$ (25 °C), $\Delta RH = 0.5$ and the water vapor density at atmospheric pressure $\rho = 0.59 \text{ kg}/\text{m}^3$, we find a new membrane moisture diffusivity:

$$D_p = 3.36 \times 10^{-12} \frac{\text{m}^2}{\text{s.Pa}} \quad (7.5)$$

Appendix C: KaysEff function

```
1 function [eff] = KaysEff(NTU_cross, NTU_counter)
2 % This function returns the effectiveness of a counter-flow
3 % heat exchanger with cross-like headers (or quasi-counterflow).
4 % Performs a Modified Akima interpolation of a 2D table, based on
5 % empirical values from Kays et al., Compact Heat Exchangers
6 % (1984). It extrapolates the effectiveness for NTU_counter>7,
7 % using eff(NTU=50)=1 as an approximation of the asymptote,
8 % to prevent the extrapolation to diverge inside the domain of
9 % study (0<NTU_counter<11; 0<NTU_cross<7).
10 % If given two vectors, the function will loop through both the
11 % vectors simultaneously and return one vector.
12 % Each column is one NTU_cross value.
13 % Each line is one NTU_counter value.
14 table =[0.000  0.476  0.615  0.682  0.723  0.752  0.773  ...
15         0.79  1;
16 0.50  0.649  0.714  0.751  0.777  0.795  0.81  0.821  1;
17 0.667  0.739  0.775  0.798  0.815  0.828  0.838  0.846  1;
18 0.75  0.792  0.816  0.831  0.843  0.852  0.86  0.866  1;
19 0.800  0.828  0.844  0.855  0.863  0.87  0.876  0.88  1;
20 0.834  0.853  0.865  0.873  0.88  0.885  0.889  0.893  1;
21 0.856  0.872  0.881  0.887  0.892  0.897  0.90  0.903  1;
22 0.875  0.886  0.893  0.899  0.903  0.906  0.909  0.912  1;
23 1  1  1  1  1  1  1  1  1]; ...
24 % Added a line of ones to approximate an asymptote
25 x = [0 1 2 3 4 5 6 7 50]; % NTU values for cross headers + big ...
26 % number to approximate the asymptote
27 y = [0 1 2 3 4 5 6 7 50]; % NTU values for counter core + big ...
28 % number to approximate the asymptote
29 eff = interp2(x,y, table, NTU_cross, NTU_counter, 'makima');
30 % 'spline' was also an option, but gave more oscillations for
31 % NTU_counter-10. 'makima' is thus our choice.
32 end
```

Appendix D: E2NTU function

```
1 function [NTU_x, NTU_c] = e2NTU_bis(eff)
2     % Gives the total number of transfer units depending on the
3     % area ratio of cross and counter part and the effectiveness. % ...
4     % Uses the interpolation/extrapolation function KaysEff to
5     % get effectiveness values for NTU_x = a * NTU_c. Then
6     % interpolation of the values using spline to get a
7     % polynomial. Then uses the Newton method to reverse it.
8
9     parameters = Parameters();
10    A_cross = parameters('A_x');
11    A_counter = parameters('A_c');
12    S_x = parameters('S_x');
13    S_c = parameters('S_c');
14    rr = 1.33659343820935; % ratio of j_x/j_c: adjustment for ratio ...
15    % when j_x is not equal to j_c
16    ratio = rr * A_cross * S_c / (A_counter*S_x);
17    NTU_c = linspace(0,20);
18    NTU_x = ratio * NTU_c;
19    NTU_tot = NTU_x + NTU_c;
20
21    corr = KaysEff(NTU_x, NTU_c);
22    pp = spline(NTU_tot, corr);
23    % spline polynomial curve fitting to the 100 points
24
25    % Newton's method to find the solution to eff = pp(NTU), NTU?
26    x0 = 0;
27    y0 = eff;
28    n = 0;
29    N = 30000;
30    step = 1e-3;
31    x = x0;
32
33    while n<N
34        fx = ppval(pp,x)-y0;
35        dfx = ((ppval(pp, x + step)-y0) - fx) / step;
36        x = x - fx/dfx;
37        y = ppval(pp,x);
38        err = abs(y0 - y)/y0;
39        if err<1e-7
40            break
41        end
42        n = n + 1;
43    end
44
45    NTU_tot = x;
46    NTU_c = NTU_tot ./ (1 + ratio);
47    NTU_x = ratio .* NTU_c;
48 end
```

Appendix E: f and j correlations for angled spacer

```
1 %% PARAMETERS & FLOW CHARACTERISTICS
2 PARAMETERS9
3
4 PD = [112.017724123325, 181.271404798645, 258.526610390003, ...
5       313.069047835164];
6 % Experimental pressure drop [Pa]
7 V_dot = [2.54 3.36 4.21 4.75]*0.001; % Volume flow rate [m3/s]
8 m_dot = rho.*V_dot; % Mass flow rate [kg/s]
9
10 b = 0.002; % Channel spacing [m]
11 a = 0.010; % Corrugation pitch [m]
12 alpha = b/a; % Aspect ratio
13 Dh = (1.0542 - 0.4670*alpha - 0.1180*alpha^2 + 0.1794*alpha^3 - ...
14       0.0436*alpha^4)*2*a*alpha;
15 % Hydraulic diameter for sinusoidal channels
16 % (Shah & Sekulic 2013, Fundamentals of heat exchanger design)
17
18 u_c = V_dot./S_c; % Velocity of air in the counter-part [m/s]
19 u_x = V_dot./S_x; % Velocity of ai in the cross-part [m/s]
20 Re_c = u_c .* Dh ./ nu; % Reynolds number in the counter-part
21 Re_x = u_x .* Dh ./ nu; % Reynolds number in the cross-part
22
23 %% FRICTION FACTOR
24
25 % Darcy Friction factor correlation from Woods (2013),
26 % spacer oriented 0 degree w/ regards to the flow direction
27 f0 = 87.2 ./ Re_c .^(0.77);
28 % Darcy Friction factor correlation from Woods (2013),
29 % spacer oriented 45 degree w/ regards to the flow direction
30 f45 = 35 ./ Re_c .^(0.49);
31 r = mean(f45./f0); % Proportionality factor
32
33 % Developing flow effect
34 Kinf = 0.674; % (Shah & Sekulic 2013, Fundamentals of heat ...
35 % exchanger design)
36 dP_dev = Kinf * (m_dot./S_x).^2 / (2*rho); % Theoretical developing ...
37 % flow effect
38
39 % Pressure drop due to bends
40 KL = 0.3904; % (Shah & Sekulic 2013, Fundamentals of heat ...
41 % exchanger design)
42 dP_bend = 2 * KL * (m_dot./S_c).^2 / (2*rho); % Theoretical bends ...
43 % effect
44
45 % Major losses
46 PD = PD - dP_dev - dP_bend;
47 % Overall friction factor
```



```

42 f = 4 * Dh * PD ./ (2*rho.*(L_c.*u_c.^2 + L_x.*u_x.^2));
43 % Friction factor separated into two parts, assuming f_x = r*f_c
44 f_c = 4 * Dh * PD ./ (2*rho.*(L_c.*u_c.^2 + r.*L_x.*u_x.^2)); % ...
    Friction factor in the counter-part
45 f_x = r.* f_c; % Friction factor in the cross-part
46
47 % Power law fit of f_c and f_x : f = C0 * Re ^ (m)
48 p = polyfit(log(Re_c),log(f_c),1);
49 m_c = p(1);
50 C0_c = exp(p(2));
51
52 p = polyfit(log(Re_c),log(f_x),1);
53 m_x = p(1);
54 C0_x = exp(p(2));
55
56 %% COLBURN FACTOR
57 %DATA 0\degree C 30%RH
58 j030_x = [0.0957    0.0840    0.0720    0.0686];
59 j030_c = [0.0716    0.0628    0.0539    0.0514];
60
61 % DATA 5\degree C 30%RH
62 j530_x = [0.1242    0.0859    0.0760    0.0735];
63 j530_c = [0.0929    0.0643    0.0568    0.0550];
64
65 % DATA 0\degree C 40%RH
66 j040_x = [0.1362    0.1081    0.0826    0.0638];
67 j040_c = [0.1019    0.0809    0.0618    0.0477];
68
69 %% COLBURN FACTOR CORRELATION
70 jmean_x = (j040_x + j530_x + j030_x)/3;
71 jmean_c = (j040_c + j530_c + j030_c)/3;
72
73 % Power law fit for j_mean : j = C1 * Re ^ (x)
74 p = polyfit(log(Re_c),log(jmean_c),1);
75 x_c = p(1);
76 C1_c = exp(p(2));
77
78 p = polyfit(log(Re_c),log(jmean_x),1);
79 x_x = p(1);
80 C1_x = exp(p(2));

```

Appendix F: MEE with “Lab” spacer

```
1 %% PROPERTIES OF THE SPACER %%
2 height = 0.002; % [m] height
3 corrugation = 0.010; % [m] corrugation pitch
4 alpha_c = height/corrugation; % aspect ratio
5 alpha_x = alpha_c;
6 Dh_c = (1.0542 - 0.4670*alpha_c - 0.1180*alpha_c^2 + ...
7         0.1794*alpha_c^3 - 0.0436*alpha_c^4)*2*corrugation*alpha_c;
8 % Dh [m] (for a sine);
9 Dh_x = Dh_c;
10
11 %% PROPERTIES OF THE FLOW %%
12 V_dot = 15.62*0.001; % [m3/s] Volume flow
13 m_dot = V_dot*rho; % [kg/s] Mass flow rate
14 % Velocity
15 u_c = V_dot./S_c; % [m/s] Velocity of the flow in the counter part
16 u_x = V_dot./S_x; % [m/s] Velocity of the flow in the cross part
17 % Reynolds number
18 Re_c = u_c .* Dh_c / nu; % Re in counter part
19 Re_x = u_x .* Dh_x / nu; % Re in cross part
20
21 %% NUSSELT NUMBER STRAIGHT
22 j_x = 9.3095*Re_c.^(-0.869);
23 j_c = 6.9651*Re_c.^(-0.869);
24 Nu_x = j_x .* Re_x .* Pr^(1/3);
25 Nu_c = j_c .* Re_c .* Pr^(1/3);
26
27 %% SENSIBLE EFFECTIVENESS STRAIGHT %%
28 NTU_c = (Nu_c.*lambda_a.*A_c) ./ (Dh_c.*m_dot*cp*2); % NTU of the ...
29         counter part
30 NTU_x = (Nu_x.*lambda_a.*A_x) ./ (m_dot*cp*2.*Dh_x); % NTU of the ...
31         counter part
32 sensible_eff = KaysEff(NTU_x, NTU_c);
33
34 %% LATENT EFFECTIVENESS STRAIGHT %%
35 rmm = Delta_m/(1.63e5*Dp);
36 k_c = (Nu_c*Le^(1/3)*Dv/Dh_c);
37 k_x = (Nu_x*Le^(1/3)*Dv/Dh_x);
38 % Number of transfer units
39 NTU_c = A_c ./ (V_dot.*(2./k_c + rmm));
40 NTU_x = A_x ./ (V_dot.*(2./k_x + rmm));
41 latent_eff = KaysEff(NTU_x, NTU_c);
42
43 %% PRESSURE DROP STRAIGHT %%
44 % Fanning friction factor experimental
45 f_x = (23.402*Re_c.^(-0.362))/4;
46 f_c = (12.922*Re_c.^(-0.362))/4;
47 % Major losses
48 dP_major_c = 2*rho*f_c.*L_c.*u_c.^2 ./ Dh_c;
```

```
46 dP_major_x = 2*rho*f_x.*L_x.*u_x.^2 ./ Dh_x;
47 % Entrance effect
48 Kc = 1.175;
49 dP_ent = Kc * (m_dot./S_x).^2 / (2*rho);
50 % Exit effect
51 Ke = -0.175;
52 dP_ext = Kc * (m_dot./S_x).^2 / (2*rho);
53 % Pressure drop due to bends
54 KL = 0.3904;
55 dP_bend = KL * (m_dot./S_c).^2 / (2*rho); % This is the theoretical ...
    bends effect
56 % Total pressure drop
57 dP_tot = dP_major_c + dP_major_x + dP_ent + 2*dP_bend + dP_ext;
```

Appendix G: Yearly savings calculation

```
1 %% YEARLY SAVINGS
2 Tset = 21; % Setpoint temperature [ degree C]
3 Tsupply = 21; % Supply temperature [degree C]
4 RHset = 40;
5 RHsupply = 40;
6 Wset = RH2W(RHset, Tset);
7 Wsupply = RH2W(RHsupply, Tsupply);
8
9 n = 8760; % number of hours counted
10
11 savings = zeros(n,1); % Vector of hourly savings
12 Q0 = zeros(n,1); % Energy consumed without MEE
13 Qtot = zeros(n,1); % Energy consumed with MEE
14 Qpre = zeros(n,1); % Energy consumed for preheating
15 Qpost = zeros(n,1); % Energy consumed for post-conditioning
16 Qfan = zeros(n,1); % Energy consumed by the fan
17
18 dP = dP_tot+system_PD; % Pressure drop of the system + MEE
19 % Energy consumed by the fan during 1 hour with MEE
20 Qfan1 = dP*V_dot*2*3600/fan_eff;
21 % Energy consumed by the fan 1 hour with bypass/without MEE
22 Qfan0 = system_PD*V_dot*2*3600/fan_eff;
23
24 for i = 1:n
25     Tout = Tout_TRD(i); % Trondheim outside temperature [degree C]
26     RHout = RHout_TRD(i); % Trondheim outside relative humidity [%]
27     Wout = RH2W(RHout, Tout);
28     frost_limit = 0; % Simplified frosting limit temperature
29
30     % Preheating
31     if Tout < frost_limit
32         Qpre(i) = (H(frost_limit, Wout) - H(Tout, Wout))*m_dot*3600;
33         Tsi = frost_limit;
34     else
35         Qpre(i) = 0;
36         Tsi = Tout;
37     end
38
39     Qfan(i) = Qfan1;
40     % Temperature and humidity after the exchanger
41     Tso = sensible_eff .* (Tset - Tsi) + Tsi;
42     Wso = latent_eff .* (Wset - Wout) + Wout;
43     RHso = W2RH(Wso,Tso);
44
45     % Post-conditioning
46     if Wout<Wset
47         Qpost(i) = (H(Tset, Wset) - H(Tso, Wso))*m_dot*3600;
```

```
48     Q0(i) = (H(Tset, Wset) - H(Tout, Wout))*m_dot*3600;
49 else
50     Qpost(i) = (H(Tset, Wso) - H(Tso, Wso))*m_dot*3600;
51     Q0(i) = (H(Tset, Wout) - H(Tout, Wout))*m_dot*3600;
52 end
53
54 % Bypass
55 if Tout > 18
56     Qfan(i) = Qfan0;
57     Q0(i) = 0;
58     Qpost(i) = 0;
59 end
60
61 Qtot(i) = (Qpre(i) + Qpost(i) + Qfan(i));
62 savings(i) = (Q0(i) + Qfan0) - Qtot(i) ;
63 end
64
65 %% CLEAR
66 clear n % Variable n is used in exterior scripts too
```

Appendix H: Parameters used in the model

```
1 % Geometrical parameters of the exchanger
2 L_c = 0.4; % Length of the counter-part [m]
3 a = 0.25; % Width of the counter part [m]
4 b = 2e-3; % Channel spacing [m]
5 L_x = sqrt(a.^2/2); % Length of the side of the cross part
6 n = 36; % Number of channels
7
8 % Calculated geometrical parameters
9 A_c = (2*n-1) * L_c .* a; % Exchange surface area counter part [m2]
10 A_x = (2*n-1) * a .^ 2 / 2; % Exchange surface area cross part [m2]
11 S_c = n * a .* b; % Channel cross-section area counter part [m2]
12 S_x = n * L_x .* b; % Channel cross section area cross part [m2]
13
14 % Properties of air (average between values for 0 degree C and 21 ...
    degree C) from
15 % www.engineeringtoolbox.com
16 cp = 1.006e3; % Specific Heat Capacity [J/(kg.K)]
17 rho = 1.24; % Density [kg/m3]
18 nu = 1.427e-5; % Kinematic viscosity [m2/s]
19 mu = 1.77e-5; % Dynamic viscosity [kg/(m.s)=Pa.s]
20 lambda_a = 2.480e-2; % Thermal conductivity [W/(m.K)]
21 Dv = 2.305e-5; % Diffusion coefficient of water vapour in air [m2/s]
22
23 % Properties of water vapor
24 cp_wv = 1859; % J/(kg.K)
25
26 % Properties of the membrane
27 Dp = 3.3609e-12; % Diffusivity [m2/s]
28 Δ_m = 3.200E-05; % Thickness [m]
29 rho_m = 3.700E+02; % Density [kg/m3]
30 epsilon = 4.100E+01; % Porosity [%]
31 lambda_m = 1.600E-01; % Thermal conductivity [W/(mK)]
32
33 % Fan efficiency
34 fan_eff = 0.125;
35 system_PD = 60;
36
37 % Non-dimensional numbers
38 Pr = cp*mu/lambda_a; % Prandtl number
39 Sc = nu/Dv; % Schmidt number
40 Le = Sc/Pr; % Lewis number
```

Appendix I: Measurement data

Case 025

Case 025: 0°C in cold room and 26% RH in exhaust air.

Flow rate 2.5 L/s			Flow rate 3.4 L/s		
Measurement	Value	Uncertainty	Measurement	Value	Uncertainty
ΔP [Pa]	109.8	± 2.4	ΔP [Pa]	179.2	± 3.3
ϵ_s [%]	90.3	± 0.8	ϵ_s [%]	94.0	± 0.4
ϵ_l [%]	94	± 9.8	ϵ_l [%]	91	± 9.4
T_{si} [°C]	13.78	± 0.092	T_{si} [°C]	13.60	± 0.034
T_{so} [°C]	21.16	± 0.055	T_{so} [°C]	21.57	± 0.027
T_{ei} [°C]	21.96	± 0.035	T_{ei} [°C]	22.08	± 0.025
T_{eo} [°C]	14.71	± 0.095	T_{eo} [°C]	14.81	± 0.027
RH_{si} [% RH]	17.0	± 1.1	RH_{si} [% RH]	16.3	± 1.1
RH_{so} [% RH]	26.8	± 1.2	RH_{so} [% RH]	25.6	± 1.2
RH_{ei} [% RH]	26.6	± 1.2	RH_{ei} [% RH]	26.4	± 1.2
RH_{eo} [% RH]	22.3	± 1.2	RH_{eo} [% RH]	21.8	± 1.2

Flow rate 4.2 L/s			Flow rate 4.7 L/s		
Measurement	Value	Uncertainty	Measurement	Value	Uncertainty
ΔP [Pa]	262.8	± 4.3	ΔP [Pa]	311.9	± 5.0
ϵ_s [%]	94.4	± 0.3	ϵ_s [%]	94.3	± 0.3
ϵ_l [%]	85	± 8.7	ϵ_l [%]	83	± 8.7
T_{si} [°C]	11.94	± 0.034	T_{si} [°C]	11.21	± 0.029
T_{so} [°C]	21.40	± 0.025	T_{so} [°C]	21.36	± 0.026
T_{ei} [°C]	21.96	± 0.025	T_{ei} [°C]	21.97	± 0.025
T_{eo} [°C]	13.41	± 0.032	T_{eo} [°C]	12.83	± 0.025
RH_{si} [% RH]	17.1	± 1.1	RH_{si} [% RH]	18.2	± 1.1
RH_{so} [% RH]	25.1	± 1.2	RH_{so} [% RH]	24.8	± 1.2
RH_{ei} [% RH]	26.9	± 1.2	RH_{ei} [% RH]	26.9	± 1.2
RH_{eo} [% RH]	23.3	± 1.2	RH_{eo} [% RH]	24.98	± 1.2

Appendix J: Measurement data Case 030

Case 030: 0°C in cold room and 30% RH in exhaust air.

Flow rate 2.5 L/s			Flow rate 3.4 L/s		
Measurement	Value	Uncertainty	Measurement	Value	Uncertainty
ΔP [Pa]	111.6	± 2.4	ΔP [Pa]	178.3	± 3.3
ϵ_s [%]	96.3	± 0.6	ϵ_s [%]	95.2	± 1.0
ϵ_l [%]	92.8	± 7.8	ϵ_l [%]	90.7	± 8.3
T_{si} [°C]	15.74	± 0.025	T_{si} [°C]	14.36	± 0.101
T_{so} [°C]	21.08	± 0.025	T_{so} [°C]	21.25	± 0.047
T_{ei} [°C]	21.29	± 0.025	T_{ei} [°C]	21.59	± 0.055
T_{eo} [°C]	16.77	± 0.028	T_{eo} [°C]	15.55	± 0.101
RH_{si} [% RH]	15.3	± 1.1	RH_{si} [% RH]	15.5	± 1.1
RH_{so} [% RH]	31.7	± 1.3	RH_{so} [% RH]	29.0	± 1.3
RH_{ei} [% RH]	32.8	± 1.3	RH_{ei} [% RH]	30.3	± 1.3
RH_{eo} [% RH]	22.4	± 1.2	RH_{eo} [% RH]	21.9	± 1.2

Flow rate 4.2 L/s			Flow rate 4.7 L/s		
Measurement	Value	Uncertainty	Measurement	Value	Uncertainty
ΔP [Pa]	255.9	± 4.3	ΔP [Pa]	312.8	± 5.0
ϵ_s [%]	94.0	± 0.9	ϵ_s [%]	93.7	± 0.3
ϵ_l [%]	85.4	± 8.4	ϵ_l [%]	81.7	± 8.1
T_{si} [°C]	12.55	± 0.040	T_{si} [°C]	11.08	± 0.034
T_{so} [°C]	21.00	± 0.053	T_{so} [°C]	21.11	± 0.025
T_{ei} [°C]	21.53	± 0.065	T_{ei} [°C]	21.78	± 0.025
T_{eo} [°C]	13.85	± 0.035	T_{eo} [°C]	12.61	± 0.029
RH_{si} [% RH]	18.1	± 1.2	RH_{si} [% RH]	18.6	± 1.2
RH_{so} [% RH]	27.6	± 1.2	RH_{so} [% RH]	26.0	± 1.2
RH_{ei} [% RH]	29.5	± 1.3	RH_{ei} [% RH]	28.4	± 1.2
RH_{eo} [% RH]	23.8	± 1.2	RH_{eo} [% RH]	25.3	± 1.2

Appendix K: Measurement data

Case 040

Case 040: 0°C in cold room and 40% RH in exhaust air.

Flow rate 2.5 L/s			Flow rate 3.4 L/s		
Measurement	Value	Uncertainty	Measurement	Value	Uncertainty
ΔP [Pa]	114.6	± 2.4	ΔP [Pa]	186.2	± 3.3
ϵ_s [%]	98.9	± 1.2	ϵ_s [%]	97.2	± 0.9
ϵ_l [%]	90.6	± 6.0	ϵ_l [%]	88.0	± 5.4
T_{si} [°C]	15.88	± 0.04	T_{si} [°C]	14.26	± 0.08
T_{so} [°C]	20.55	± 0.04	T_{so} [°C]	19.76	± 0.04
T_{ei} [°C]	20.61	± 0.04	T_{ei} [°C]	19.92	± 0.03
T_{eo} [°C]	16.79	± 0.042	T_{eo} [°C]	15.26	± 0.081
RH_{si} [% RH]	15.0	± 1.1	RH_{si} [% RH]	15.5	± 1.1
RH_{so} [% RH]	38.5	± 1.3	RH_{so} [% RH]	40.2	± 1.3
RH_{ei} [% RH]	41.2	± 1.3	RH_{ei} [% RH]	43.8	± 1.4
RH_{eo} [% RH]	24.7	± 1.2	RH_{eo} [% RH]	25.93	± 1.2

Flow rate 4.2 L/s			Flow rate 4.7 L/s		
Measurement	Value	Uncertainty	Measurement	Value	Uncertainty
ΔP [Pa]	256.9	± 4.3	ΔP [Pa]	314.5	± 5.0
ϵ_s [%]	95.1	± 0.5	ϵ_s [%]	93.2	± 2.0
ϵ_l [%]	83.8	± 5.1	ϵ_l [%]	81.7	± 7.9
T_{si} [°C]	12.34	± 0.05	T_{si} [°C]	11.25	± 0.04
T_{so} [°C]	19.22	± 0.03	T_{so} [°C]	19.62	± 0.11
T_{ei} [°C]	19.57	± 0.03	T_{ei} [°C]	20.23	± 0.14
T_{eo} [°C]	13.45	± 0.052	T_{eo} [°C]	12.57	± 0.032
RH_{si} [% RH]	17.7	± 1.1	RH_{si} [% RH]	18.9	± 1.1
RH_{so} [% RH]	40.8	± 1.3	RH_{so} [% RH]	35.9	± 1.7
RH_{ei} [% RH]	45.5	± 1.4	RH_{ei} [% RH]	40.0	± 1.9
RH_{eo} [% RH]	27.95	± 1.2	RH_{eo} [% RH]	29.32	± 1.3

Appendix L: Measurement data

Case 530

Case 530: 5°C in cold room and 30% RH in exhaust air.

Flow rate 2.5 L/s			Flow rate 3.4 L/s		
Measurement	Value	Uncertainty	Measurement	Value	Uncertainty
ϵ_s [%]	98.3	± 1.4	ϵ_s [%]	95.4	± 1.0
ϵ_l [%]	91.0	± 8.6	ϵ_l [%]	91.0	± 9.0
T_{si} [°C]	17.62	± 0.03	T_{si} [°C]	16.45	± 0.05
T_{so} [°C]	21.19	± 0.04	T_{so} [°C]	20.99	± 0.03
T_{ei} [°C]	21.25	± 0.04	T_{ei} [°C]	21.21	± 0.03
T_{eo} [°C]	18.43	± 0.028	T_{eo} [°C]	17.26	± 0.049
RH_{si} [% RH]	19.03	± 1.2	RH_{si} [% RH]	19.7	± 1.2
RH_{so} [% RH]	33.7	± 1.3	RH_{so} [% RH]	32.1	± 1.3
RH_{ei} [% RH]	35.4	± 1.3	RH_{ei} [% RH]	33.3	± 1.3
RH_{eo} [% RH]	25.6	± 1.2	RH_{eo} [% RH]	25.05	± 1.2

Flow rate 4.2 L/s			Flow rate 4.7 L/s		
Measurement	Value	Uncertainty	Measurement	Value	Uncertainty
ϵ_s [%]	94.5	± 0.6	ϵ_s [%]	94.2	± 0.6
ϵ_l [%]	84.6	± 8.6	ϵ_l [%]	80.9	± 8.1
T_{si} [°C]	15.22	± 0.06	T_{si} [°C]	14.28	± 0.04
T_{so} [°C]	20.67	± 0.03	T_{so} [°C]	20.45	± 0.03
T_{ei} [°C]	20.99	± 0.03	T_{ei} [°C]	20.83	± 0.03
T_{eo} [°C]	16.12	± 0.054	T_{eo} [°C]	15.30	0.042
RH_{si} [% RH]	21.04	± 1.2	RH_{si} [% RH]	22.27	± 1.2
RH_{so} [% RH]	31.3	± 1.3	RH_{so} [% RH]	31.6	± 1.3
RH_{ei} [% RH]	33.6	± 1.3	RH_{ei} [% RH]	34.7	± 1.3
RH_{eo} [% RH]	26.10	± 1.2	RH_{eo} [% RH]	28.5	± 1.2

Appendix M: Effectiveness- RH_{ei} regression

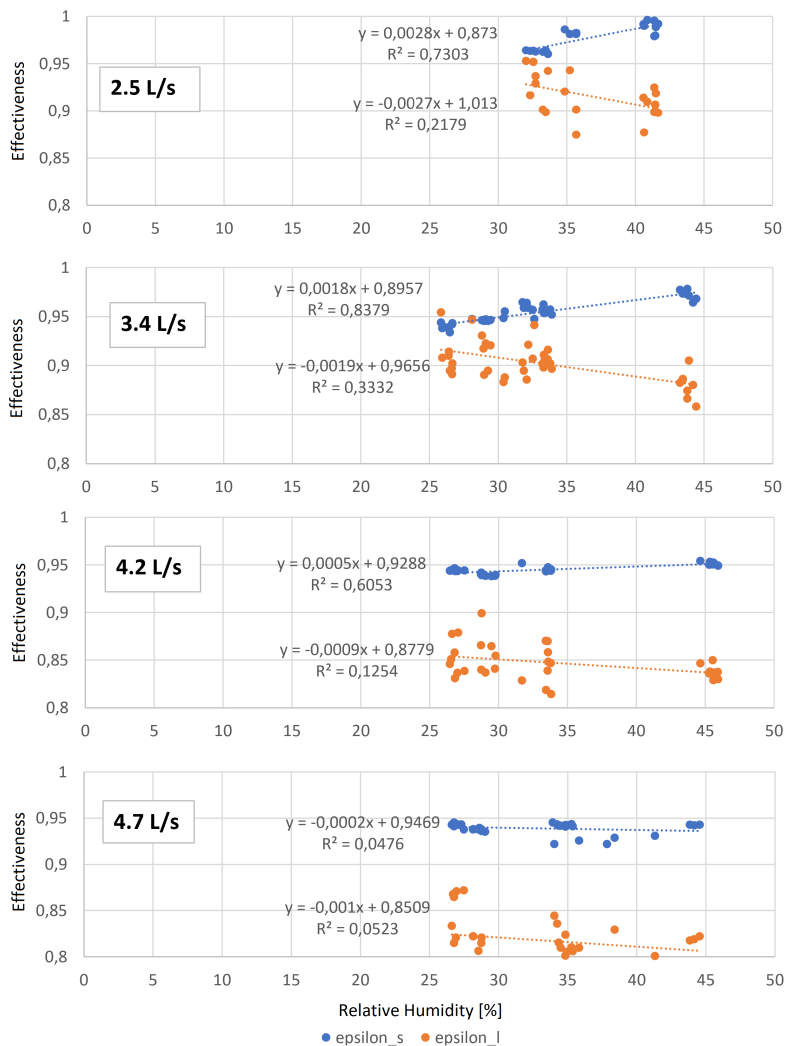


Figure 7.1: Linear regression for effectiveness versus RH_{ei}

